EXPERIMENTAL OBSERVATION AND MEASUREMENTS OF POOL BOILING HEAT TRANSFER USING PIV, SHADOWGRAPHY, RICM TECHNIQUES

A Thesis

by

YUAN DI

Submitted to the Office of Graduate Studies of
Texas A&M University
in partial fulfillment of the requirements for the degree of

MASTER OF SCIENCE

Approved by:

Chair of Committee,	Yassin A. Hassan
Committee Members,	William H. Marlow
	Kalyan Annamalai
Head of Department,	Yassin A. Hassan

December 2012

Major Subject: Nuclear Engineering

ABSTRACT

This present study seeks to contribute detailed visualization data on a pool boiling experiments using HFE-7000. Particle Image Velocimetry (PIV) was used to measure the time resolved whole field liquid velocity. Bubble dynamic parameters such as nucleation site density, bubble departure diameter, contact angles and frequency were obtained in shadowgraphy measurements. Infrared thermometry with an IR camera was used for observation of temperature fluctuations of nucleation sites. The experiments were taken for the heat flux from 0.042 kW/m^2 to 0.266 kW/m^2, six experimental conditions in total.

To provide a supplementary description of heat transfer mechanism, a novel bubble characterization technique, reflection interference contrast microscopy (RICM), was used to obtain detailed information on bubble dynamic parameters on the microscopic scale. Bubble diameter was obtained from RICM pictures.

Comparison between the experiments results and previous empirical correlation were made. Agreements and discrepancies were discussed.

DEDICATION

To my parents

ACKNOWLEDGEMENTS

I would like to thank my committee chair, Dr. Hassan, and my committee members, for their guidance and support throughout the course of this research.

Also I would like to thank my friends and colleagues and the department faculty and staff. All of you had made my time at Texas A&M University a great experience. I also want to extend my gratitude to my group members. Thanks for your help and support in the experiments especially the experimental setup. It was a great time working with you. I learned a lot of new ways of experimental design ideas. Without your kind help, there is no way I can finish this experiments.

Finally, thanks to my parents and friends for their encouragement and patience and love.

TABLE OF CONTENTS

Page

ABSTRACT ii

DEDICATION iii

ACKNOWLEDGEMENTS iv

TABLE OF CONTENTS v

LIST OF FIGURES vii

LIST OF TABLES x

1. INTRODUCTION 1

1.1 Nucleate Pool Boiling Fundamentals 2
1.2 Nucleate Pool Boiling Experiments 5
1.3 Two-Phase Flow Visualization Techniques 6
1.3.1 PIV and PTV Techniques 6
1.3.2 Infrared Thermometry 7
1.3.3 X-Ray Radiography 7
1.4 Reflection Interference Contrast Microscopy Method 8
1.5 This Work 9

2. EXPERIMENTAL BASED THEORY 10

2.1 PIV Algorithm Description 10
2.1.1 Object (particle) Detection and Particle Centroid Determination 11
2.1.2 Particle Tracking 14
2.1.3 Velocity Field Calculation 15
2.2 RICM Technique Description 16
2.2.1 RICM Theory 17
2.3 Infrared Thermometry 20

3. POOL BOILING EXPERIMENTS 25

3.1 Pool Boiling Experiments Facility Description and Capabilities 27
3.1.1 Experimental Facility Overview 27
3.1.2 Hydraulic Loop 27

3.1.3 Visualization System 29
3.1.4 Heating Element Design 31
3.1.5 Power Supply and Working Fluid and Seeding Particles 36
3.2 Experiments Procedure 37

4. DATA PROCESSING AND RESULTS 40

4.1 PIV Data Processing and Results 40
4.2 Bubble Shadowgraphy Data Process and Results 45
4.2.1 Data Analysis Process 45
4.2.2 Results Discussion 52
4.3 Infrared Measurement Results Analysis 55

5. RICM MEASUREMENT AND IMAGE PROCESSING 59

5.1 RICM Test Facility 59
5.2 Image Process and Height/Shape Reconstruction 61
5.2.1 Min/Max Method 62
5.2.2 The Refractive Index Method 63
5.3 Height Reconstruction with Known Symmetric Shape 64
5.4 RICM Images Results and Discussion 67

6. CONCLUSIONS 76

6.1 Summary 76
6.2 Lessons Learned 76

REFERENCES 78

LIST OF FIGURES

Page

Figure 1	Physical interpretation of boiling curve (Farber)	3
Figure 2	RICM Principle Scheme[26]	18
Figure 3	Basic principle of RICM, interference fringes result from the different optical path these two beam rays I1 and I2 travel.	19
Figure 4	Suppressing stray light principle	20
Figure 5	Temperature distribution through ITO heater	22
Figure 6	IR calibration experiment setup	23
Figure 7	IR calibration correlation	23
Figure 8	Temperature difference through the ITO heater	24
Figure 9	The schematic of pool boiling facility	26
Figure 10	Photograph of pool boiling facility	26
Figure 11	FLIR systems, SC8200 IR camera	30
Figure 12	ITO heater schematic graph	31
Figure 13	Infrared camera picture of the ITO heater	33
Figure 14	Temperature profile of x axis	33
Figure 15	Improved heater temperature field	34
Figure 16	Temperature profile along x axis	34
Figure 17	Transmissivity spectrum of borosilicate glass substrate from Bayview Optics. Inc	35
Figure 18	Transmissivity spectrum of ITO from Bayview Optics. Inc	36

Figure 19 Examples of PIV measurement images 38

Figure 20 Examples of shadowgraphy images 39

Figure 21 Liquid velocity fields at different wall heat flux. (1) to (6) is the velocity field with the heat flux increasing, referring to the test matrix in Table 1. 40

Figure 22 Laser induced heat effects 43

Figure 23 Laser induced new nucleation sites at the wall heat flux of 0.11 kW/m^2 44

Figure 24 (a) is the original image, (b) is the inverted image. It is similar for (c) and (d), except that (c) and (d) are background images without any boiling happening 47

Figure 25 An example of final image, using inverted raw images subtracting inverted background images 47

Figure 26 Define area of interest, from which the time=dependent intensity profiles is obtained, which is used as input of later frequency analysis 48

Figure 27 Bubble departure frequency results from shadowgraphy experiments with different heat flux 49

Figure 28 Bubble departure frequency vs. wall heat flux 51

Figure 29 Bubble departure diameter vs. wall heat flux 52

Figure 30 Bubble departure diameter v.s. wall super heat by previous experimental correlations, concluded by Craig Geradi [34] 53

Figure 31 Previous pool boiling experiments data conclusion by Craig Geradi [34] 55

Figure 32 Grey scale profile from infrared images 57

Figure 33 Nucleation sites density vs. wall heat flux 58

Figure 34 ITO heater schematic drawing 60

Figure 35 RICM facility close look 60

Figure 36 RICM experiments setup 61

Figure 37 RICM image processing procedure[26] 62

Figure 38 Triple interface interference 63

Figure 39 RICM Surface reconstruction principle scheme[26] 67

Figure 40 Background picture of nucleation site 68

Figure 41 (a) is the intensity analysis process. (b) is the intensity profile in radial direction 69

Figure 42 Grey scale profiles in radial direction, 3 measurements 70

Figure 43 Distance between adjacent extrema on the RICM image fringe patterns 72

Figure 44 Bubble Surface Reconstruction 74

Figure 45 Fitting curve enlargement view 74

LIST OF TABLES

Page

Table 1 Test matrix of the PIV and shadowgraphy experiments 38

Table 2 Wall overheat under different heat flux 58

Table 3 Distance between two adjacent extremas on fringes 72

Table 4 Surface reconstruction parameters 73

Table 5 Surface height increments v.s. radial positions 73

1. INTRODUCTION

There is a lot of study about the pool boiling phenomena. It is a very effective mechanism of heat transfer. There are many applications in both science and industries. However, there is little research on subcooled pool boiling. It is of great importance in nuclear engineering industry, since coolant inside the PWR primary loop are kept in subcooled condition. Moreover, for decades, research on pool boiling heat transfer has been restricted to empirical science. Most of the research focused on the experimental studies, concluding many empirical correlations. As research advanced these days, the demand for high-quality, high resolution data of pool boiling two phase parameters is increasing. It is important to visualize the bubble behavior and the liquid near the heating surface to clarify the details concerning boiling mechanism. Such information will also provide valuable validation basis for high resolution CFD simulations.

This present study seeks to contribute detailed experimental data on bubble dynamic parameters such as nucleation site density, bubble departure diameter, contact angles and frequency, as well as time-resolved whole-field liquid temperature and velocity measurements, and the time history of the liquid micro-layer thickness change. Particle image velocimetry (PIV), bubble shadowgraphy and reflection interference contrast microscopy (RICM) techniques are to be used in this work to get measurement and observation of heat transfer mechanism at different scales. PIV and shadowgraphy measurements are adopted to obtain the time resolved bubble-liquid field behaviors.

1.1 Nucleate Pool Boiling Fundamentals

When liquid is in contact with a heating surface with temperature higher than the fluid saturation temperature, boiling will occur at the liquid solid surface[1]. Such boiling phenomenon is divided into two categories based on the relative movement between the bulk fluid and the heating surface; pool boiling and convective boiling. When the heater is immerged in a large bulk of fluid, the boiling is usually referred as pool boiling. The relative motion between the bubbles and surrounding liquid near the heating surface is mainly determined by the net forces acting on the bubbles, mainly the buoyancy force from the bubble, the surface tension on the bubble, etc. However, the main body of liquid is assumed stagnant. Pool boiling has wide application in various aspects in industry.

In spite of its wide application, there are few theoretical descriptions of pool boiling mechanisms. The properties of liquid and vapor, surface material and heater size are all inter-dependent variables that make the theoretical descriptions difficult. There is no consensus on which heat transfer mechanisms are dominate during the bubble.

There is study on the effect of large wall super heat, ΔT by Nukiyama[2]. Most of the characteristics of classical pool boiling curve were determined. However, until 1948, Farber and Scorah[1] studies the heat transfer rate in the pool boiling. Their experiments were conducted in water at different pressures, using a cylindrical wire as heater. The heater is inserted in the water horizontally. From the results, the boiling curve was divided into 6 regions, as shown in Figure 1.

If the power is the controlled variable instead of a controlled wall temperature, then wall heat flux increase in Region III results in an abruptly transitions from nucleate boiling to the film boiling regime at the critical heat flux, a point in Region VI. This heat flux at the transition point is called the critical heat flux and it is important in pool boiling phenomena. The sudden increase of wall temperature will sometimes damage the heater. For most engineering systems, this sharp rise in temperature is approximately 1000 ℃, which is large enough to melt or destroy the heated surface. In this case, the critical heat flux is referred to as the burnout heat flux, and typically represents a design limit for an engineered system.

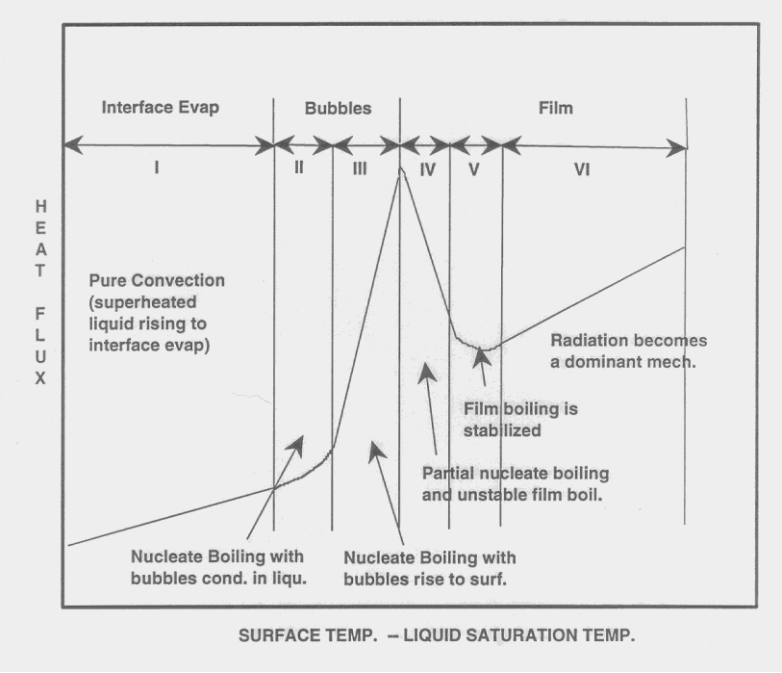

Figure 1 Physical interpretation of boiling curve (Farber)

Several bubble parameters are crucial in nucleate pool boiling, including nucleation site density, bubble departure diameter and bubble departure frequency. A brief discussion of these parameters is as follows.

The number of nucleation site increase with the increase of wall heat flux. However, no exact theoretical models had been proposed because of lack of information of the number and shape of micro-cavities present on typical engineering surfaces. Kocamustafaogullari and Ishii [3]developed a correlation using the wall superheat as, $N_{sd} \propto \Delta T_{sat}^{m_1}$, where m_1 varies between 4 and 6. Wang and Dhir [4] developed a mechanical way of estimating the nucleation site density. This method depends on the cavity information such as, size, shape and mouth angle.

The bubble departure diameter is determined by the net effect of forces acting on bubble, mainly interfacial surface tension and the buoyancy force. The buoyancy force tends to pull up the bubble, while the interfacial force tends to hold the bubble back to the heating surface. Besides, the wall superheat, contact angle and two phase thermo-physical properties also affect the bubble departure diameter. There are various kinds of empirical correlations about the bubble departure diameter. Many people, such as Zuber[5] , Ruckenstein[6], Cole and Rohsenow[7], had developed models for the bubble departure diameter. However, there is a large discrepancy between different correlations.

Bubble departure frequency depends on the bubble departure diameter considering the growth and size of bubbles. Each nucleation site has its own size and characteristics, which will affect the bubble growth and wait times, thus results in different departure frequencies. Jakob and Fritz [8] proposed a simple relationship

between bubble frequency and diameter. While Peebles and Garber[9] included the influence of bubble growth time and wait time. Zuber and Cole took the drag force into consideration.

1.2 Nucleate Pool Boiling Experiments

There are many experiments carried out to measure the pool boiling parameters. Various two phase flow measurements techniques are adopted focusing on different aspects of pool boiling phenomenon. Of all the parameters concerned, the bubble dynamic parameters such as bubble diameter, bubble departure frequency and nucleation site density is of great importance in the pool boiling phenomena. Moreover, the bubble growth time, departure time and temperature profiles of the heater surface are also important.

However, the measurement of nucleation site density has always been a problem. Most of the attempts made are intrusive, and highly variable. Gaertner and Westwater [10] found that the nucleation site density is proportional to the square of heat flux. Wang and Dhir [4] recorded 1 cm^2 area of heater surface by still photography, using degassed, sub-cooled (5-10K) water as working fluid. Their heater was mirror finished copper, so it can yield a range of contact angles. They found the CHF increases and nucleation site density decrease with wetting. Based on the data from Gaertner-Westwater and pre-existing models, Kocamustafaogullari and Ishii [3]obtained the minimum cavity mouth radius required for activation. Using the data from Borishanskii [11], they deduced a different expression for the nucleation site cavity size. T.G. Theofanous and J.P. Tu [12] used a novel approach of infrared thermometry to obtain the visualization of dynamic

temperature profiles of the heater's surface. Such kind of experimental data was firstly presented.

1.3 Two-Phase Flow Visualization Techniques

1.3.1 PIV and PTV Techniques

Visualization techniques such as Particle Image Velocimetry (PIV) and Particle Tracking Velocimetry (PTV) can be used to overcome some of the limitation of the traditional two phase measurement techniques. Both PIV and PTV are non-intrusive methods. Using high speed high resolution cameras, instantaneously time resolved whole field flow information can be obtained. By analyzing the images from PIV experiment, the positions of particle tracers seeded in the fluid could be obtained. With the know time interval between consecutive images, instantaneous fluid velocities can be obtained. The small tracers are assumed to follow the motion of the fluids closely. That's why tracers which density approach the fluid most and with enough small sizes are chosen in the measurements.

The major difference between PIV and PTV measurements lies in the concentration of the tracers. In PIV measurements, the concentration of tracers is relatively high, in order to capture the local fluid velocity field. The velocity field is averaged over many particles in certain volume. For PTV measurement, a single particle tracer is tracked to obtain the velocity. Although there are different between two techniques, the basic principles behind the track methods are similar. Thus, both techniques can be applied in two phase flow.

1.3.2 Infrared Thermometry

For the measurements of temperature field, other than the traditional thermocouples, a novel technique is introduced, that is infrared thermometry. Due to the high frequency nature of the boiling phenomenon, it is important to have high speed imaging and storing capability. The early trial of using infrared thermometry dates back to the early 70s. Myers's group used infrared camera to study the nucleation pool boiling with thin heater plates[13]. Later, Kenning [14] improved the technique and obtained some results at low heat flux in nucleate boiling. It was not until 2000s that infrared-based thermometry of temperature field on heated surfaced was introduced by Theofanous et al.[12] Such kind of thermometry was used to obtain a time and space-resolved temperature field. Craig Gerardi [15] had used this thermometry for pool boiling phenomena in study nanofluids in water.

1.3.3 X-Ray Radiography

Besides infrared thermometry, researchers also made use of the X-ray radiography to measure two phase flow parameters. Such technology is based on the principle that X rays will attenuation in matters. X-ray's attenuation factor is different in different matters. By comparing the intensity of X-rays before and after passing through certain matter, two phase flow patterns in pool boiling.

From previous literature, very few trials were made to measure void fractions in pool boiling. Ida and Kobayasi [16] used conductivity probes to measure the local void fraction. Liaw and Dhir [17] used a densitometer to detect attenuation of a gamma beam with a vertical heated surface. However, all the previous measurements results are

restricted to the local point void fraction, and usually, the values were averaged over certain period of time intervals. Nowadays, the need is more focusing on obtaining time resolved void fraction field in two phase flow.

1.4 Reflection Interference Contrast Microscopy Method

In the study of bubble dynamics in pool boiling, it is of great interest to study the property of microlayer between bubbles and the heating surface. Theoretically, from the patterns of interference, the surface information such as the separation height from the bottom surface and curvature could be obtained. In the 1980s Sackmann and co-workers started applying the closely related technique of "Reflection Interference Contrast Microscopy" or RICM to surfaces such as those of colloidal beads or membranes[18]. The image obtained from the camera is intensity profiles variation on 2D plane. With proper mathematical analysis, the relation between positions and their corresponding height separation from the bottom can be determined. The vertical height separation resolution of the measurement can go down to nanometer scale. With the application of modern digital cameras and fast data storage, RICM techniques have been applied to a variety of engineering phenomena.

Over the years, there have been some crucial improvements of the RICM techniques. One of the important advances is the introduction of dual (and later multi)-wave RICM [19]. This technique can identify the phase related to any interference technique, and makes the absolute height measurements possible. Such improvement makes the surface and height reconstruction more precise. Another important improvement was that using symmetric characteristics in the fringe patterns, the surface

reconstruction accuracy can be greatly improved.[20]. With multi-interface analysis, the absolute height could be determined. These improvements make RICM a promising method for micro scale surface interaction studies.

When bubbles are formed from the cavity on the heater surface, the process involves the bubble surface interaction with the liquid phase. Thus, it is natural that the exploration of applying RICM techniques in the pool boiling measurements. If successful, detailed information from a much micro scale could be obtained. The RICM experimental theory and image process theory were described in detailed in the following sections.

1.5 This Work

This present study seeks to contribute detailed data on bubble dynamic parameters such as nucleation site density, bubble departure diameter, contact angles and frequency, as well as time-resolved whole-field liquid temperature and velocity measurements, and the time history of the liquid micro-layer thickness change. Particle image velocimetry (PIV), shadowgraphy and reflection interference contrast microscopy (RICM) techniques are to be used in this work to get measurement and observation of heat transfer mechanism at different scales. Some satisfying preliminary results have been obtained, and future work will focus on improvement of RICM measurements and PIV measurements. Such information is a valuable development and improvement of interfacial transport models used in CFD calculations.

2. EXPERIMENTAL BASED THEORY

In this pool boiling experiments, particle image velocimetry (PIV) technique was used to measure the liquid phase flow field. To obtain the bubble dynamics parameters not provided by PIV, bubble shadowgraphy was adopted. In addition to these two techniques, infrared thermometry by IR camera was tried to get the temperature profile of the heating surface in an attempt to obtain more information about the nucleation sites, together with the data from PIV and shadowgraphy. Moreover, a novel technique reflective interference contrast microscopy (RICM) was adopted to get more detailed information about the bubbles from a much micro scale. In this section, the theoretical bases of these visualization techniques were briefly introduced.

2.1 PIV Algorithm Description

Particle image velocimetry (PIV) is a method of getting high quality, high resolution two phase flow information from complicated flows by tracking particles tracers seeded in the flow. Flow visualization with PIV involves seeding the fluid with particles. Using particle tracers whose density resembles that of the fluids, it is assumed that the particle tracers could track the movement of liquid flow. One form of PIV measurement is performed by illuminating the fluid with a thin sheet of pulsed laser light and then recording images of the particles moving in the flow with high speed cameras. This is called pulsed laser velocimetry (PLV).[21] The goal of PIV is to quantitatively measure large numbers of vectors over the full-field. An algorithm's ability to track

complicated flows must be verified. Error analysis in PIV tracer tracking program should be performed using synthetic data.

To measure the liquid phase velocity field in the pool boiling experiments, an in-house developed particle tacking algorithm was adopted. This algorithm was originally developed by Cannan and Hassan.[22] And there have been many improvements over the years. Basically, the particle tracking method involves two major steps, first, object identification, along with the centroid position determination and then object matching. In the end, the velocity vector field could be obtained. In this thesis, a brief discussion of particle tracking techniques is as follows. The more detailed description could be found in other literature. The tracking program used in this work is a home-made software based on VB.net.[21]

2.1.1 Object (particle) Detection and Particle Centroid Determination

Accurate identification and detection of objects are extremely important in multi-phase flow experiment. In the PIV images, the seeded particle tracers should be the targeted objects. Bubbles and background should be discriminated from particles tracers in the algorithm. Particle parameters, such as size, shape could be used for discrimination. In this work, the analysis code applies the particle mask correlation method in particle detection. Such method was discussed in detail by Takehara[23].

The mask particle tracking method could identify not only the centroid of the objects, but also to identify the pixels that belong to the object. With proper threshold values, this method can be used as a filter in identifying the similar areas through the sweeping through the interrogation areas. The cross correlation coefficient was

computed using the intensity of both the mask area and the target interrogation areas, as represented as C1.

Objects with certain area will have certain brightness patterns depending on the specific models applied. Normally, the intensity pattern of a particle image has a strongest intensity value peak in the center, and the intensity profile decreases with the increase of distance from the center. In this work, a 2-D Gaussian distribution was proposed to mathematically represent the intensity pattern of the particle image. Usually, it is an ideal particle image generated from the following equation.

$$I(x,y) = I_0 exp[-\frac{1}{2r_0^2}(\frac{(x-x_0)^2}{A^2} + \frac{(x-x_0)(y-y_0)}{c^2} + \frac{(y-y^2)^2}{B^2})] \quad (1)$$

This equation applies a Gaussian representation of an ideal particle where $I(x,y)$ is the gray scale intensity on the (x,y) position. (x_0,y_0) is the particle centroid location. I_0 is the maximum intensity in the object area. r_0 is the particle radius. a, b, and c are shape modifier parameters. By selecting a small value of r_0, particle tracers can be discriminated from bubbles. Background areas are usually darker than the particle tracer and bubbles areas, in this way, using proper intensity threshold values, background area can be discriminated. For different areas of locations, different values of shape modifier parameters are chosen. The comparison of different shape modifier parameters effects are shown in other literature. [21]

Typically, the particle mask correlation method has the following steps:

First, the cross correlation coefficients were calculated. The cross correlation coefficient between the object mask and the interrogation area in the image plane is calculated using the following equation:

$$C_1(x_0, y_0) = \frac{\sum_{i=x_0-a}^{x_0+a} \sum_{j=y_0-a}^{j=y_0+a} (I(i,j)-\hat{I})(I_m(i,j)-\hat{I}_m)}{\sqrt{\sum_{i=x_0-a}^{i=x_0+a} \sum_{j=y_0-a}^{j=y_0+a} (I(i,j)-\hat{I})^2} \sqrt{\sum_{i=x_0-a}^{i=x_0+a} \sum_{j=y_0-a}^{j=y_0+a} ((i,j)-\hat{I}_m)^2}} \quad (2)$$

Here $C_1(x_0, y_0)$ is the cross correlation coefficient at the centroid location (x_0, y_0), $I(x, y)$ is the intensity value of particle image plane at (i, j), and $I_m(i, j)$ is the brightness value of the particle mask. (i, j) is the serial number of interrogation areas in the adjacent PIV image. $\hat{I}$ and $\hat{I}_m$ are average intensities of the interrogation area and the object mask image, respectively. After sweeping the whole plane, the cross correlation values were calculated for each interrogation areas on the image, varying from -1 to 1. The cross correlation coefficient value determines how similar the interrogation area at the (i, j) location is, comparing to the original mask area. By setting proper threshold values, the next possible locations of the objects could be determined.

In related studies, two kinds of thresholds are considered. The gray scale threshold (GST), and mask cross correlation coefficient threshold (C_1T). Interrogation areas having gray scale values and correlation coefficient larger than these thresholds are candidates to be part of an object. The values of these thresholds will depend on the application. If the centroid location of objects is studied, the only necessary threshold is the C_1T. On the other hand, if the size of the objects is also a concern, the GST value must be chosen. In this work, since liquid phase velocity fields are concerned, which means only the objects position is important, the C_1T is a major concern.

2.1.2 Particle Tracking

After a pixel is determined to be part of an object, the next step is to determine to which object this pixel belongs. In other word, the object should be related to the last image, for the calculation of object velocity vector. This procedure is done by the top-left sweeping algorithm. The particle tracking algorithm used in this study is based on direct spatial correlation.[21]

It is well known that largest part error in PIV data processing comes from the object centroid location determination. In the mask cross correlation technique, pixel position was calculated only where the object centroid is located. The total number of pixel unites used in this algorithm is integer. In order to reduce the error resulted from centroid location, better methods are introduced. In this way, better determination of object centroid location could reduce the error in PIV studies. Usually, there are three different centroid estimation techniques available: three point Gaussian interpolation (3PGI)[24], two dimensional Gaussian regression (2DGR)[25], and center of mass technique (CMT). All these methods have sub-pixel interpolation accuracy. The former two techniques are suitable for small Gaussian shaped objects, while the CMT technique is suitable for larger objects with no shape restriction. In this way, CMT will be ideal for bubbles centroid location. In this work, 2DGR is used, since it integrates more information in estimation. Nine points are used in the regression rather than six points. However, 3PGI technique is the most commonly used.

Consider (x_0, y_0) to be the pixel position with a higher C_1 value within an object. By adding the sub-pixel correction ε_x for x coordinate and ε_y for y coordinate, the centroid location of the object is determined. Using 3DGR interpolation, the ε_x and ε_y are expressed as follows:

$$\varepsilon_x = \frac{\log(I(x_0-1,y_0))-\log(I(x_0+1,y_0))}{2\log(I(x_0-1,y_0))+\log(I(x_0+1,y_0))-2\log(I(x_0,y_0))} \tag{3}$$

$$\varepsilon_y = \frac{\log(I(x_0,y_0-1))-\log(I(x_0,y_0+1))}{2\log(I(x_0,y_0-1))+\log(I(x_0,y_0+1))-2\log(I(x_0,y_0))} \tag{4}$$

So the particle centroid position with sub-pixel accuracy (x_c, y_c) is expressed as follows:

$$x_c = x_0 + \varepsilon_x \tag{5}$$

$$y_c = y_0 + \varepsilon_y \tag{6}$$

However, if the calculated sub-pixel corrections ε_x or ε_y are greater than 1.0 or smaller than -1.0, the interpolation is considered as a failure, and the CMT is used instead, where

$$\varepsilon_x = \frac{\sum_{k=1}^{K} x_k I(x_k,y_k)}{\sum_{k=1}^{K} I(x_k,y_k)} \tag{7}$$

$$\varepsilon_y = \frac{\sum_{k=1}^{K} y_k I(x_k,y_k)}{\sum_{k=1}^{K} I(x_k,y_k)} \tag{8}$$

And K is the total number of pixels in the object.

2.1.3 Velocity Field Calculation

After the pairing of objects is successful, the position of all the objects in frame j and in frame j+1 is known. Recalling that the time intervsal between these frames,ΔPIV, the velocity component could be calculated as follows:

$$u_i = \frac{dx_i}{dt} = \frac{x_{i2} - x_{i1}}{\Delta PIV} \quad (9)$$

$$v_i = \frac{dy_i}{dt} = \frac{y_{i2} - y_{i1}}{\Delta PIV} \quad (10)$$

Where u_i and v_i represent the velocities in the stream-wise and normal flow direction of object i. x_{i2} and x_{i1} represent the x coordinate position of object I in frames j, and $j + 1$ respectively, and y_{i2} and y_{i1} represent the y coordinate positions of object i in frame j and $j + 1$ respectively.

2.2 RICM Technique Description

To provide a supplementary description of heat transfer mechanism, a novel bubble characterization technique, reflection interference contrast microscopy (RICM), was used to obtain detailed information on bubble dynamic parameters on the microscopic scale. RICM is a technique originally developed to characterize the adhesion of particle to glass surface. When a monochromatic light incident from the bottom of the objects, it will interfere with the reflected light ray from the surface of the object, forming interference fringes. This is how the RICM images are formed. In this case, inducing monochromatic light from the bottom of the heating surface, light rays reflected from the surface of the bubble and the heating surface will interfere and form fringes. After an approximated fringe spacing analysis, the bubble geometry could be obtained.

In this section, the basic principal of RICM measurements together with the method of image processing (absolute surface height and shape reconstruction) is discussed in detail.

2.2.1 RICM Theory

The optical theoretical basis for RICM technique is shown in Figure 2 . When a monochromatic light incident from the bottom of the objects, it will interfere with the reflected light ray from the surface of the object, forming interference fringes. From the figure, we know that when a monochromatic beam of light I_0 incident from the bottom of the plate, there will be two rays of reflection light. First the glass/medium interface will reflect part of the light, gives the ray, I_1; while the transmitted ray will then be reflected at the surface of the object, forming ray I_2. I_1 and I_2 will interfere and combine to a total intensity$I$. The intensity of I is described by the following equation.

$$sI = I_1 + I_1 + 2\sqrt{I_1 I_2}\cos[2kh(x,y)cos\vartheta + \emptyset] \quad (11)$$

Where, $k = {}^{2\pi n_1}/_{\lambda}$ and $\emptyset$ is the phase change, $h(x,y)$ is the height between the bubble and glass substrate at lateral position(x,y). The figure below shows the intensity I profiles on the glass substrate, which in case of pool boiling bubbles are concentric fringes.

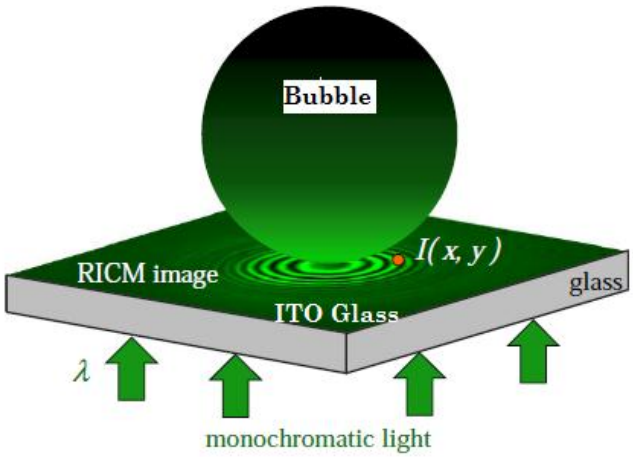

Figure 2 RICM Principle Scheme[26]

Using the simplest form of Equation (11), using $\emptyset = \pi$, one could rewrite the equation and get the intensity of combined intensity of reflected light.

$$2I = S - Dcos\left(\frac{4\pi n_1}{\lambda}h\right) \tag{12}$$

Where S and D is the sum and difference of the maximum intensity I_{max} and I_{min}, respectively. Here, $I_{max} = I_1 + I_2 + 2\sqrt{I_1 I_2}$ and $I_{max} = I_1 + I_2 - 2\sqrt{I_1 I_2}$. Here the intensities $I_1$and I_2 can be deduced from I_0, using Fresnel reflection coefficient.

$$I_1 = r_{01}^2 I_0 \tag{13}$$

$$I_2 = (1 - r_{01}^2) r_{12}^2 I_0 \tag{14}$$

Here r_{ij}^2 is called Fresnel reflection coefficient $r_{ij}^2 = \frac{n_i - n_j}{n_i + n_j}$ $(i, j = 0.1.2)$.

Thus, the RICM yields a holographic picture of the surface profile of microscopic objects. The 3-D reconstruction of the surfaces can be carried out by image processing, and only surfaces close to the substrate can be investigated. [27]

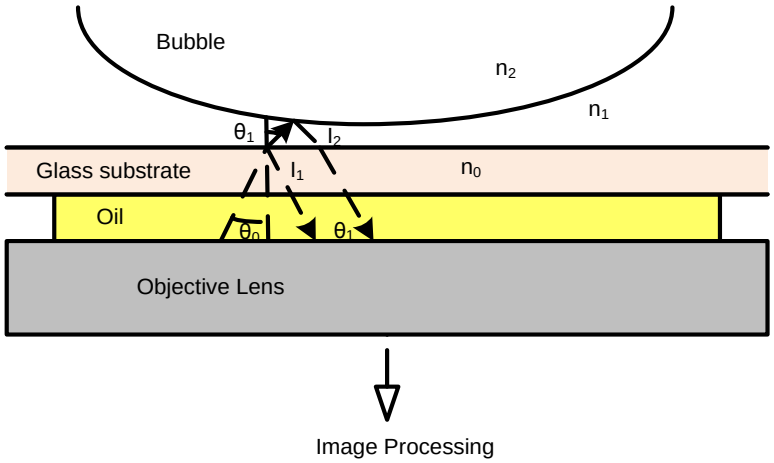

Figure 3 Basic principle of RICM, interference fringes result from the different optical path these two beam rays I_1 and I_2 travel.

Usually, the intensity of reflected monochromatic light is very low (10^{-3} I_0) and the observation of fringe patterns is usually obscured by stray light. Thus, the reflection contrast, also called antiflex technique, is adopted to reduce the stray light. [28] As shown in Figure 3 and Figure 4, the principle of reflective contrast is introduced. Light becomes polarized after passing the polarizer P_l and it illuminate the objects. The microscope objective is covered with a $\lambda/4$ plate. The light becomes circular polarized after passing through the objective. The reflected light passes the $\lambda/4$ plate again and becomes linear polarized again, but turned by 90° with respect to the illumination beam. In this way, the object beam could pass the crossed analyzer P_A placed in the observation path, while the stray light will be blocked.

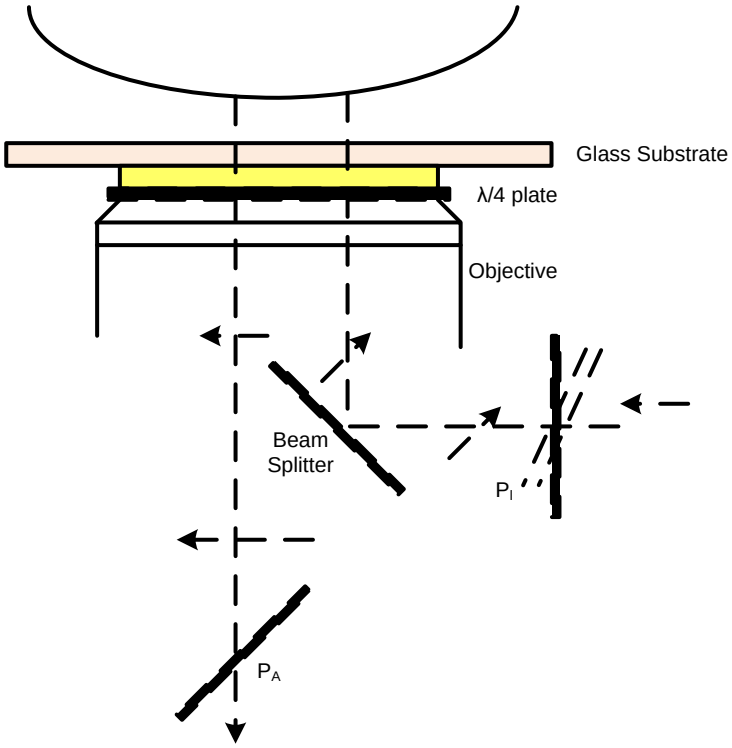

Figure 4 Suppressing stray light principle

2.3 Infrared Thermometry

Infrared thermography[29] is a kind of non –intrusive method of temperature measurement. Infrared or near infrared radiation emitted from the objects were detected by the infrared sensors. In this way, a fast response, instantaneous temperature field could be obtained. The infrared radiation was first brought up by Sir Isaac Newton in 1866, when he was doing the experiment of dispersion of light. Later, many scientists did a lot of research to measure the energy of infrared radiation.

Now from the blackbody radiation theory, we know that the infrared radiation energy from an object is in an amount proportional to the fourth power of its temperature. The Stefan-Boltzmann Law, or Stefan's Law clearly states the radiation

energy flux rate from blackbody with absolute temperature T, as shown in above1Equation (15).

$$j^* = \sigma T^4 \tag{15}$$

This is the foundation of infrared thermometry. In the real world, in order to calculate the infrared energy emitted using blackbody radiation theory, the parameter "emissivity" is introduced as a correction. Emissivity is a ratio of gray body emission to that from a blackbody emission at the same temperature. Here, the emissivity of the gray body is assumed constant with respect to wavelength.

When the object was viewed by the infrared camera, objects with different temperature will emit infrared light with different energy and different wavelength, so that the infrared camera could easily discriminate these objects. With a certain frame rate, the infrared camera could capture the dynamic process of temperature profiles of area of interest.

In this work, a SC8200 infrared camera from FLIR system., Inc, was used. This camera has the resolution of 1024×1024, and the maximum frame rate of 132 Hz with full window. If the measuring window is reduced, the frame rate can be increased. The temperature within the range of -20℃ to 500 ℃ (-4°F to 932 °F).

It is obvious that the measurement value from IR camera cannot be used as the object actual temperature, because of the error due to variation of emissivity, reflectivity, and transmissivity of ITO-heater. More importantly, in the pool boiling experiments, IR camera was measuring the glass side temperature. Due to conduction through the glass

and convection heat loss on the glass side, there will be a temperature drop through the glass, as shown in Figure 5.

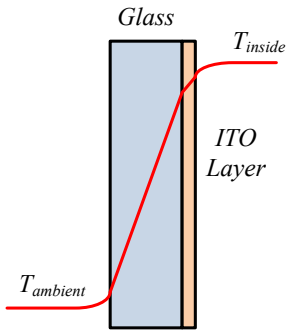

Figure 5 Temperature distribution through ITO heater

In order to infer the actual temperature on the surface of ITO-heater, the correlation from a series of simple experiments were estimated. The temperature range of interest is from 30℃ to 70℃. By comparing the measurements results from E-type thermocouples and the experimental values from IR camera, the correlation is concluded. In this test, IR camera was set at a frame rate of 131.5 Hz with the spatial resolution of 1024 ×1024. The experimental set up is shown in Figure 1. The IR camera was placed in front of a ITO heater. The heater was connected to a DC power supply. E-type thermocouples was used to measure the real temperature of heater surface.

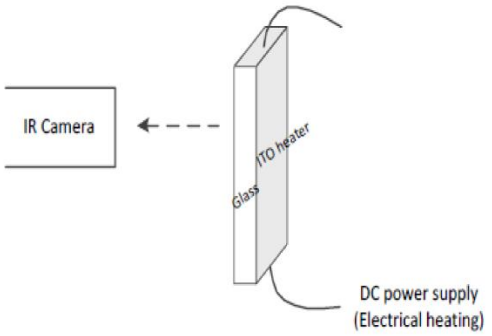

Figure 6 IR calibration experiment setup

Totally, 3 sets of data were measured in the small calibration test. The correlation between the IR measurement results and the actual temperature from E-type thermocouples is shown in

Figure 7. Experimental results were expressed in dots. Black lines are fitting curves. After averaging, the relation is expressed as follows:

$$T_{actual} = 0.92353 * T_{IR} + 1.19243 \quad (16)$$

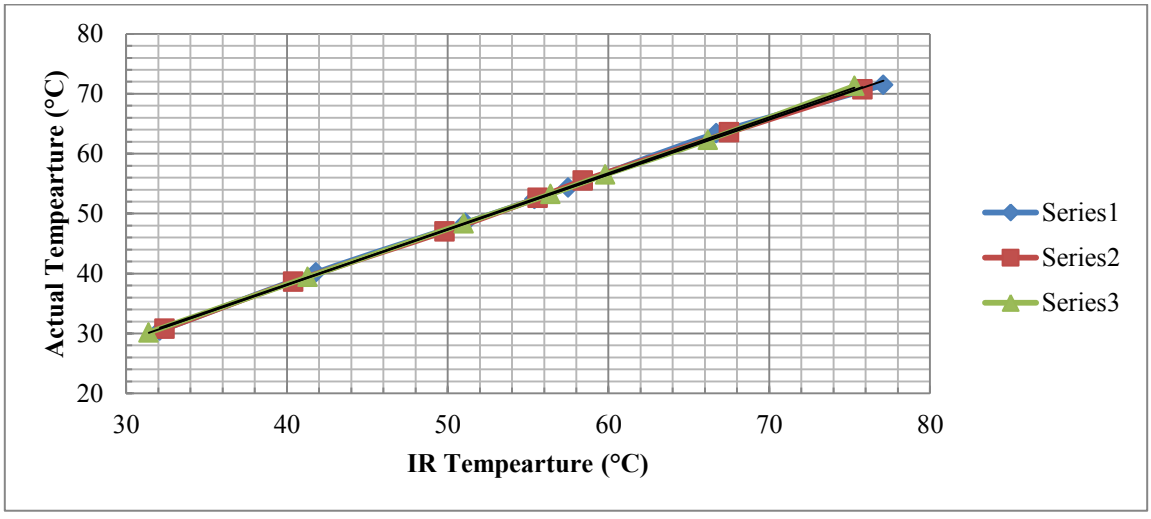

Figure 7 IR calibration correlation

In order to correct the temperature drop throughout the ITO heater glass, another small test was perform to get the correlation of temperatures on different side of ITO heater. Two identical E-type thermalcouples were placed on different side of the ITO heater. Under different heat flux, the measurement values from these two thermocouples were compared. The linear fitting was used to obtain its correlation, as shown in Equation (17).

$$T_{inside} = 1.0097 \times T_{actural} + 0.0373 \quad (17)$$

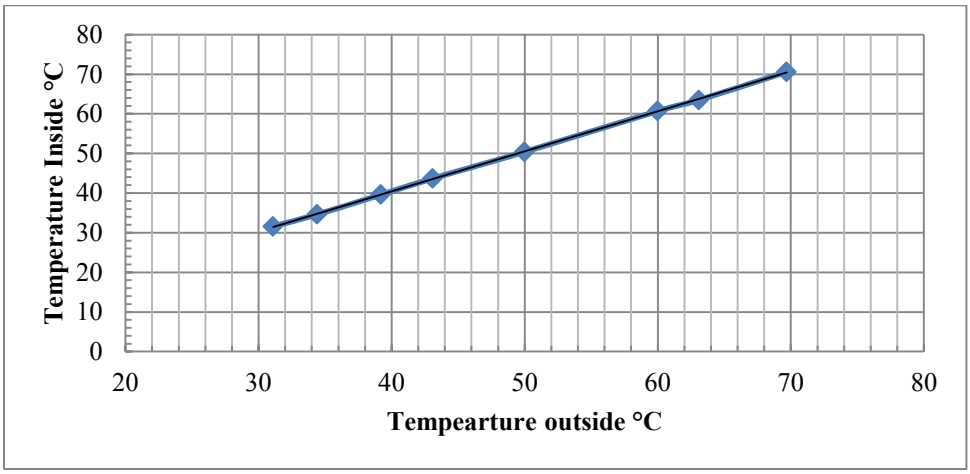

Figure 8 Temperature difference through the ITO heater

3. POOL BOILING EXPERIMENTS

In this chapter, the pool boiling facility was discussed in detail from the set up stage to the experimental procedure. The fabrication of the ITO heater and how it is set up in the facility is crucial for the success of the pool boiling experiments. In this experiment, we started to gain some first experience about how to use the infrared camera to capture the temperature field of heating surface. Moreover, a lot of experience had been learned from setting up of the facility, which is valuable for future heat transfer experiments, such as subcooled flow boiling experiments. The results of the test are analyzed in the reminder of this thesis to give a picture of the pool boiling two phase field. The schematic of pool boiling facility is shown in Figure 9, and a photograph of the facility is in the following figure.

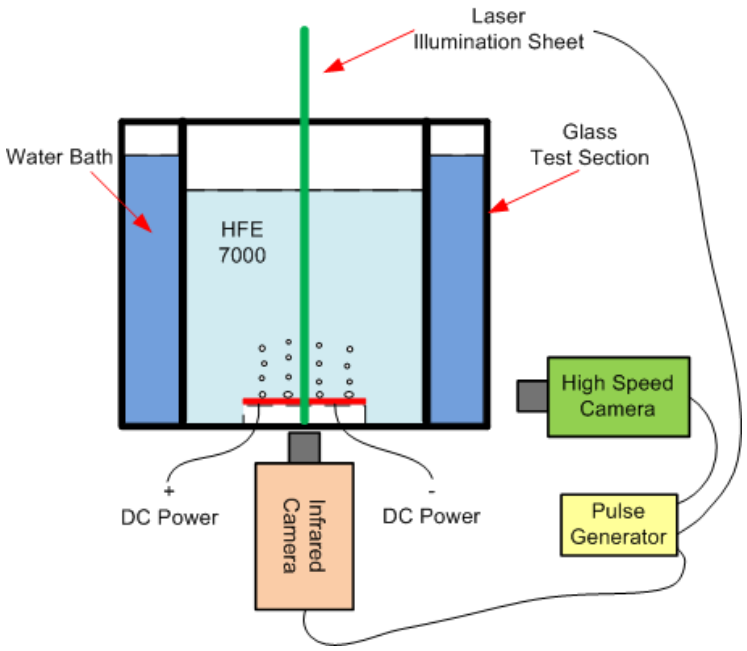

Figure 9 The schematic of pool boiling facility

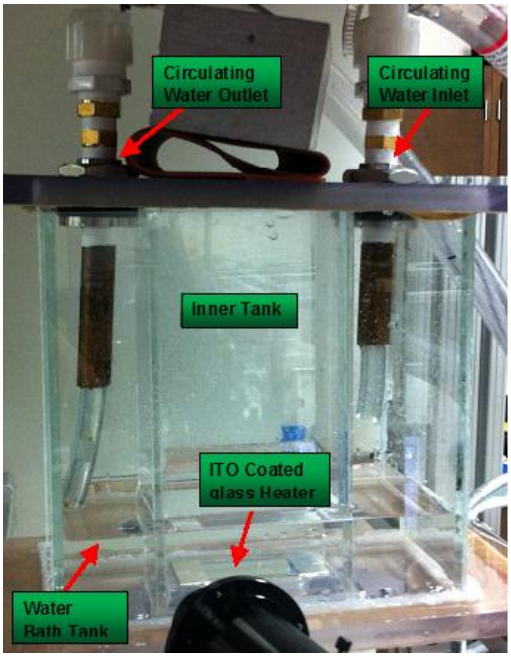

Figure 10 Photograph of pool boiling facility

3.1 Pool Boiling Experiments Facility Description and Capabilities

3.1.1 Experimental Facility Overview

The pool boiling facility was used in PIV and shadowgraphy experiments, aiming to obtain the space and time resolved two phase flow field in pool boiling. Shadowgraphy measurements could get the bubble dynamics parameters, such as bubble departure diameter, bubble departure frequency, etc. The PIV measurement could get the liquid phase information around the bubbles. A high speed camera was used to capture the dynamics of the pool boiling process. Moreover, an infrared camera was used in an attempt to obtain the dynamic temperature profile of the heating surface. The experimental facility consists of a hydraulic loop and a visualization system. More detailed descriptions are in the following sections.

3.1.2 Hydraulic Loop

The hydraulic loop in the pool boiling facility consists of the test section and an external circulating loop with cooling water. The external loop consists of piping, fitting, valves, a constant temperature circulation water tank with circulation pump, and an outer tank of the testing section. The external loop was filled with circulating cooling water to with varying temperature from 10℃ to 34 ℃ for different experimental conditions.

The test section consists of two rectangular glass tanks. Both the inner tank and the outer water bath tank are made out of transparent Starphire glass, with wall thickness of 5mm. This kind of glass has a good transmissivity for the 532nm green laser light. The inner tank is the test section. Its dimension is 10cm×5cm×20cm (length ×width ×height). An outer isothermal bath tank serves to maintain the entire facility below the

saturation temperature of the refrigerant (34℃) throughout the duration of each experiment. The Novec 3M 7000 Fluid was chosen as the working fluid because of its unique thermal and mechanical properties. All the component materials are chosen to be compatible with the working fluid. The test chamber was designed at the atmospheric pressure of 1 atm. The outer tank was used similar to the water bath, to keep the inner test tank temperature constant for different experimental conditions. Loss of fluid in the inner tank by evaporation is minimized by maintaining a quasi-seal on the top of the tank. The top lid prevents most of the steam leakage, but it is loose enough to keep the test tank at atmospheric pressure.

Energy for the pool boiling was provided by a borosilicate glass covered with Indium-Tin-Oxide (ITO) layer. Only a strip area of approximate 142 mm^2 is covered with the ITO layer. Such pattern is to eliminate the bubbles from generating from the side, enabling most of the nucleation sites are within the camera view. The reason why such fabrication was adopted is discussed in the following section. The maximum working temperature of the heater is approximately 200 ℃. To reduce heat losses to the environment, hard paper was used to cover the around the test facility. However, still, the heat loss by radiation and convection is not negligible. Such loss is discussed in detail in the reminder of the thesis. By connecting the ITO heater to the DC power supply, from which a series of heat flux were achieved, from 0.042127 kW/m^2 to the maximum heat flux of 0.266493 kW/m^2. By Joule heating, pool boiling occurred on the surface of the ITO film.

To monitor the temperature of the heating surface and the bulk fluid temperature in the pool, two K-type thermal couples are placed inside the test section pool. One is placed near the heating surface; the other was in the bulk tank. Moreover, to record the temperature fluctuation of the heater surface, infrared thermometry with IR camera was used by measuring the infrared light intensity. Synchronized with the high speed camera by pulse generator, the dynamic process of boiling was captured.

3.1.3 Visualization System

The visualization system consists of flow particles tracer, a high speed camera, a high frequency, high power laser for PIV experiments, a halogen lamp for shadowgraphy experiments, lenses and mirrors, other supportive tracks.

A kind of highly reflective silver coated particles was selected as the flow tracer for PIV measurements. Such kind of particles has a density range of 1.39 to 1.41 g/cm^3. Such density range is preferred since it is almost the same with the working fluid of HFE 7000, which density is 1.4 g/cm^3. When under heated situation, the particles would suspend in the bulk fluid, tacking the movement of liquid phase. Its diameter is about 40μm. The illumination source for the PIV experiments is a 527nm laser source. In the shadowgraphy experiment, the illumination source is a continuous halogen lamp.

The maximum frame rate of high speed camera is 7000 frames per second at a maximum resolution of 800×600 pixels. The spatial resolution of the camera is μm/ pixel. In the PIV experiments, the high speed camera was synchronized with the laser source through a pulse generator. The illumination source was provided by a twin pulsed Nd-Yag laser with green light wavelength of 527 nm. Optical reflective mirror and

concave-convex lenses are used to convert the small circular beam from the laser source into a thin sheet of light. In the experiment, the laser sheet is positioned through the mid-plane of the tank from one side, shinning perpendicular to the ITO heater surface in order to illuminate the particles above the heater. The camera was positioned perpendicular in front of the tank compared to the laser sheet. The lenses, mirrors and cameras are mounted to the movable tracks, so that their relative positions could be adjusted for better focus onto the measurement region.

For the shadowgraphy measurements, similar the PIV video acquisition system, the same high speed camera was used. Instead of high frequency laser beam source, a continuous halogen lamp was used for illumination.

To acquire the temperature fluctuation profile of the ITO heater surface, an infrared camera was used to measure IR intensity from the bottom of the pool boiling facility. The IR camera was a SC8200 IR camera from FLIR systems, Inc, as shown in Figure 11.

Figure 11 FLIR systems, SC8200 IR camera

3.1.4 Heating Element Design

In this facility, the transparent ITO heater was chosen. Boiling occurs on the upward facing side of the ITO layer. The schematic and photograph of the heater is shown in Figure 12.

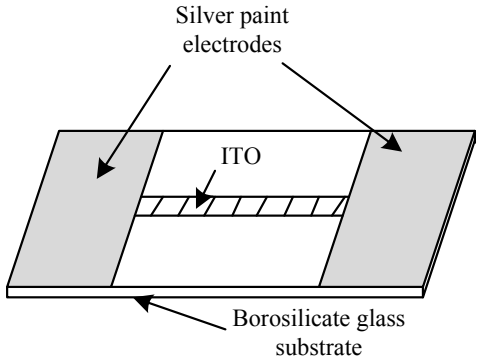

Figure 12 ITO heater schematic graph

The ITO was deposited onto the borosilicate substrates. The substrate was 1.1 mm thick. The heater was made by Bayview Optics company in Maine, US. The ITO layer deposited on the glass substrates has the resistance of 10 Ohms/Square with the thickness of 1500 Angstroms. Usually, the actual resistance of the heater is slightly higher which is due to slight difference in the manufactured ITO thickness and properties.

As shown in the schematic figure of the ITO heater, silver electrodes were used for connecting to the DC power supply. Because of the high thermal conductivity and low electric resistance of the silver metal, the temperature hot spot will not be located at the areas of the electrodes. At first, we attempted to deposit pure silver onto the ITO surface to fabricate the electrodes. About 100 nm thick of silver was deposited onto the

ITO surface by metal evaporation technique. However, the pure silver layer is easily peeled off the surface. Then we found an easier way to fabricate the electrodes. A reliable conductive silver paint from Ted Pella, Inc. was applied. Leitsilber[30] is a fast drying and has a flat surface texture, normally used in SEM specimens. The silver content is 45%, with a resistance of 0.02-0.04 Ohms/Square. Its maximum surface temperature is 120 ℃. The silver paint can be easily applied to the ITO heater surface by brush. Pre-tests have shown that the surface is smooth enough to eliminate cavities from becoming potential nucleation sites.

As for the connection of the heater to the DC power supply, copper wires were fixed onto the silver electrodes by double sided adhesive, electrically highly conductive carbon tapes. Such kind of tape was specially designed for attaching samples to be examined by SEM. Since the surface of the tape is porous, the silver paint was applied on top of the tape after attaching the copper wire to the heater surface.

Small tests were performed using infrared camera to make sure the preferred temperature profiles is achieved. Connecting to the DC power supply, the ITO heater was placed in front of the IR camera. Figure 13 and Figure 14 shows the temperature profile of heating surface. This is the profile when the ITO heater was glued to the bottom of the inner test tank by UV epoxy.

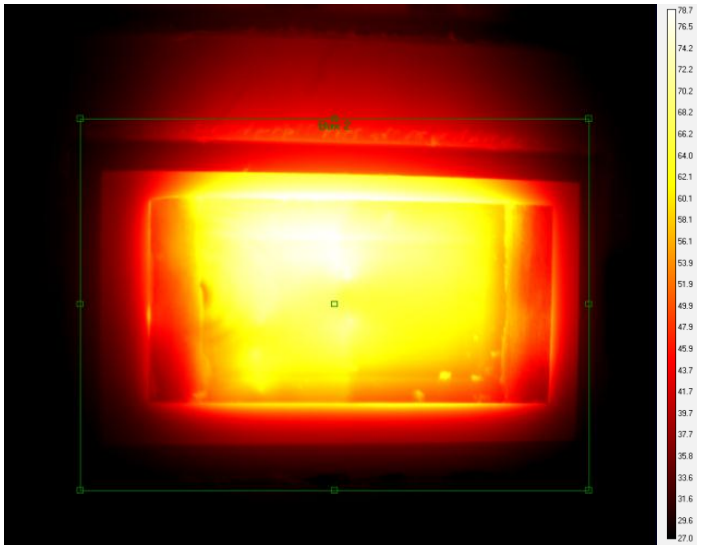

Figure 13 Infrared camera picture of the ITO heater

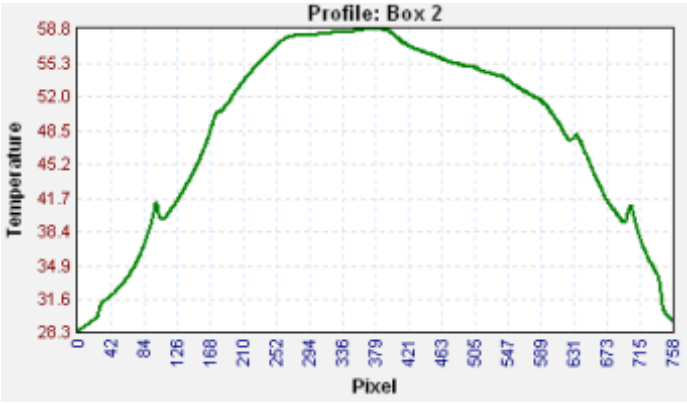

Figure 14 Temperature profile of x axis

In the pool boiling experiments, the nucleation sites are preferred to locate in the central area of the heater for easier observation by the cameras. Thus, the above profile is not ideal. Then the ITO layer was etched to only a thin strip at the center. The infrared camera temperature profile validation figure is shown below in Figure 15 . In Figure 16,

we can see the temperature profile is almost flat in the central area, which means a nearly uniform heat flux is achieved.

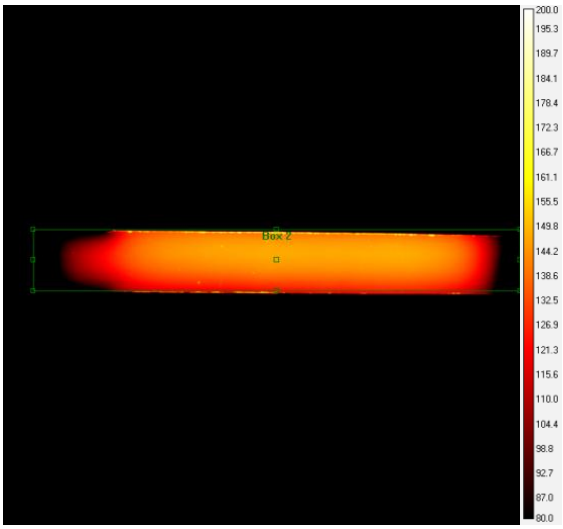

Figure 15 Improved heater temperature field

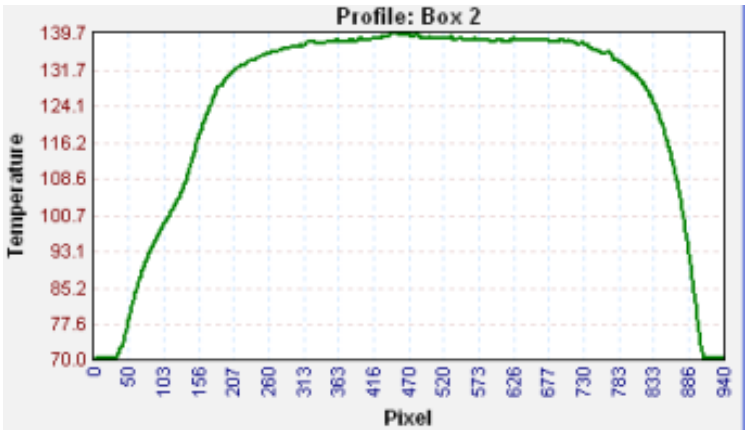

Figure 16 Temperature profile along x axis

Since IR thermometry is used in the experiments, the transmissivity of ITO and borosilicate glass is important. The borosilicate substrate is transparent in visible (380-750 nm) and mid-IR (3-5 μm) spectrums. The glass substrate transmission spectrum is

shown in Figure 17, from Bayview Optics. The transmission spectrum of ITO used in this experiment is shown in Figure 18, from Bayview Optics. The poor transmissivity of ITO layer is extremely important in estimation of temperature in IR thermometry. Ideally, sapphire substrate should be used for the reason that it has higher transmissivity in the mid-IR range than borosilicate glass. However, due to the limitation of time and resources, ITO heater with borosilicate substrate was firstly used. With similar method and experience gained in this attempt, more accurate results can be obtained in the future easily. If sapphire substrate was used, with its relatively higher transmissivity in mid-IR range, coupled with the poor transmissivity of ITO layer, temperature measurements can be made on the bottom of the ITO heater. In this way, neither the temperature of the fluid, nor the integral temperature through the substrate thickness is measured.

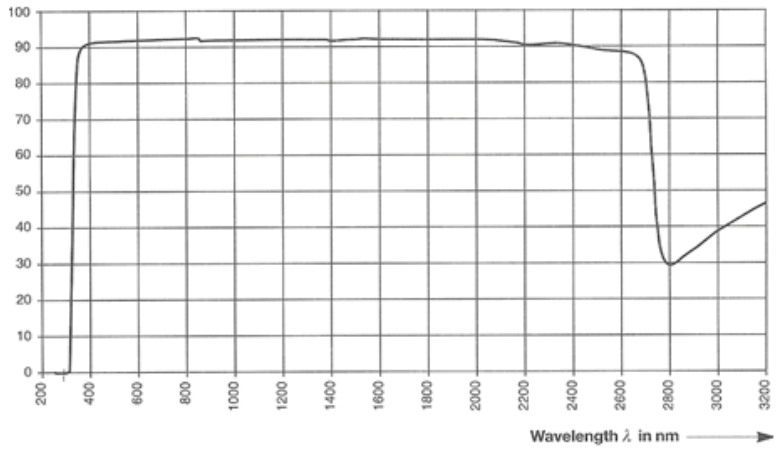

Figure 17 Transmissivity spectrum of borosilicate glass substrate from Bayview Optics. Inc

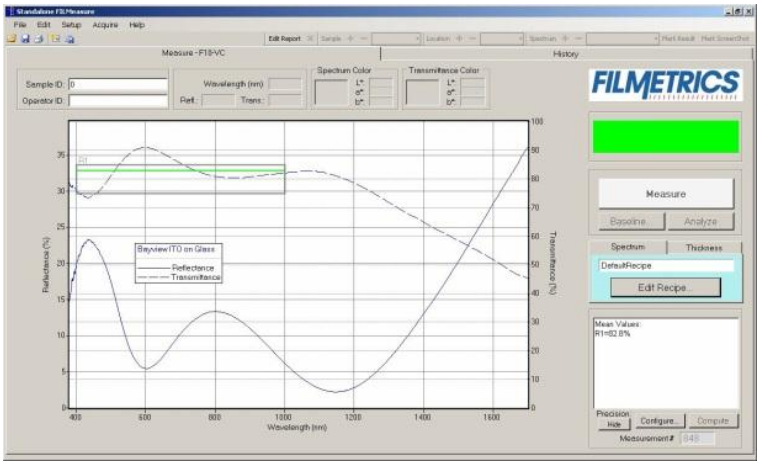

Figure 18 Transmissivity spectrum of ITO from Bayview Optics. Inc

3.1.5 Power Supply and Working Fluid and Seeding Particles

The power supply used in this work has a maximum voltage of 50 V and a maximum current of 25 A. The Novec 3M 7000 Fluid was chosen as the working fluid because of its unique thermal and mechanical properties. [31]

As stated before, a kind of highly reflective silver coated particles from Dantec Dynamics[32] was selected as the flow tracer for PIV measurements. This is a spherical silver coated borosilicate glass particle with a density of 1.4 g/cm^3 and a diameter between 2-20 μm. The density resembles the density of the refrigerant, which are 1.34 g/cm^3. However, from the results of later analysis, it is found that such particles are not ideally suitable. It is found that a lot of the particles were deposited after experimental measurements. That is due to the density decrease of fluid by heating. Thus, particles with smaller density should be used in future experiments. In future tests, hollow glass spheres are found to be more suitable. The hollow borosilicate glass particle (HGS) has a same size distribution of 2-20 μm, but with a much smaller density of 1.1 g/cm^3.

3.2 Experiments Procedure

The PIV and bubble shadowgraphy measurements were carried out for 6 different heat flux conditions, from 0.042 kW/m^2 to 0.266 kW/m^2. In the PIV measurements, the visualization system is equipped with a laser as an illumination source for the high-resolution/high-speed that is to be placed perpendicular to the laser sheet plane.

In the PIV measurements, the camera was positioned to focus the surface of the ITO heater. The camera was synchronized with a high energy laser. The laser sheet is 1mm thick, used for illumination. The camera frame rate was set at 2000 frames/s, with an exposure time of 2 μs. Each image acquired consisted of 600×800 pixels. For each pixel in the image, it represents 0.2822 mm in realtity. For each different heat flux, water bath temperature was kept at 20℃. For each case, 4398 pictures were acquired. The experimental matrix is shown in Table 1.

To ensure the inner pool bulk temperature is below the boiling point of working fluids, T-type thermocouples were used as validation.

The heater energy was provided by a DC power supply, with varying voltage and current. Due to heat loss from the bottom of the ITO heater, the actual heat flux from the inner surface of the pool tank should be modified. Assume that the heat loss from the outer surface heater is purely due to free air convection. Radiation is neglected since temperature difference between the heater and environment is not large. And assume the heat convection transfer coefficient is constant. So, the actual wall heat flux was estimate using the following assumption:

$$q''_{inner} = q''_{total} - \propto (T_{out} - T_{in}) \quad (18)$$

Table 1 Test matrix of the PIV and shadowgraphy experiments

Current (A)	Voltage(V)	Power(W)	q''_{total} (kW/m^2)	T_{in} (K)	T_{out} (K)	q''_{inner} (kW/m^2)
0.10	7.7	0.77	0.054127092	301.45	300.25	0.042127
0.15	10.2	1.53	0.107551236	306.25	300.25	0.047551
0.20	13.1	2.62	0.184172704	312.45	300.25	0.062172
0.25	16.3	4.075	0.28645182	317.85	300.25	0.110451
0.30	19.3	5.79	0.407007617	324.35	300.25	0.166007
0.35	22.7	7.945	0.55849318	329.45	300.25	0.266493

Figure 19 represents example pictures of the unheated single-phase flow images in PIV measurements. We could easily identify the seed particles from the black background. Combining the measurement pictures together with the black background, the time resolved liquid fluid velocity profile could be estimated. The principle and step by step process of liquid velocity field estimation was discussed in detailed in the reminder of this thesis.

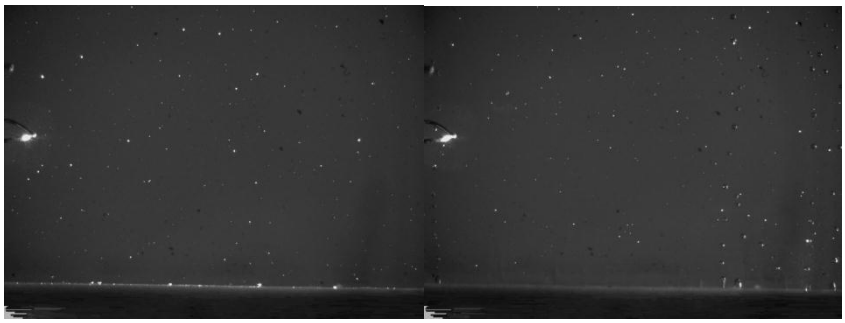

Figure 19 Examples of PIV measurement images

In supplement to PIV measurements, bubble shadowgraphy measurements were carried out to obtain the description of bubble dynamics in two phase flow. Similar to the PIV visualization system, a light bulb instead of the laser was used to illuminate the system. In order to be consistent with PIV measurements, shadowgraphy measurements were carried out under the same experimental conditions. Figure 20 represents an example of the bubble shadowgraphy results, with varying heat flux from 0.0421 kW/m^2 to 0.266 kW/m^2.

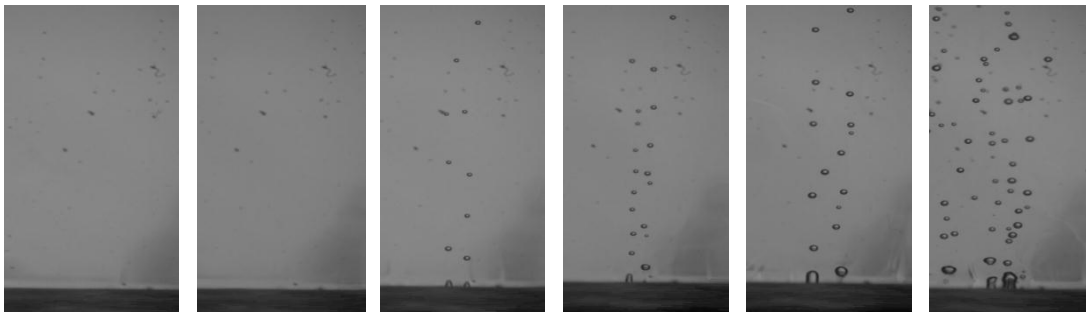

Figure 20 Examples of shadowgraphy images

4. DATA PROCESSING AND RESULTS

4.1 PIV Data Processing and Results

For each of the 6 different experimental conditions, a clip of video was recorded. The water bath temperature was kept at 20 ℃. To ensure the pool bulk temperature is below the boiling point of refrigerant, T-type thermocouples measurement results were listed in Table 1. Each video tape was then broken down to 4398 frames of pictures, with the time interval of 0.5 ms between two consecutive pictures. A home developed program was used for analysis. The principle of the software was discussed in detail in the previous section.

Using the code described in the previous section, raw images were processed. The liquid field is obtained under different heat flux in Figure 21.

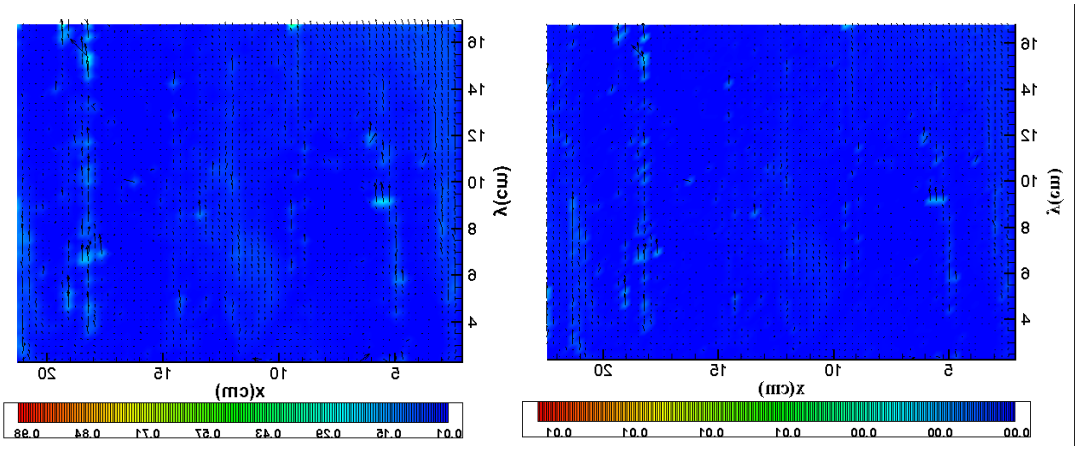

(1) (2)

Figure 21 Liquid velocity fields at different wall heat flux. (1) to (6) is the velocity field with the heat flux increasing, referring to the test matrix in Table 1.

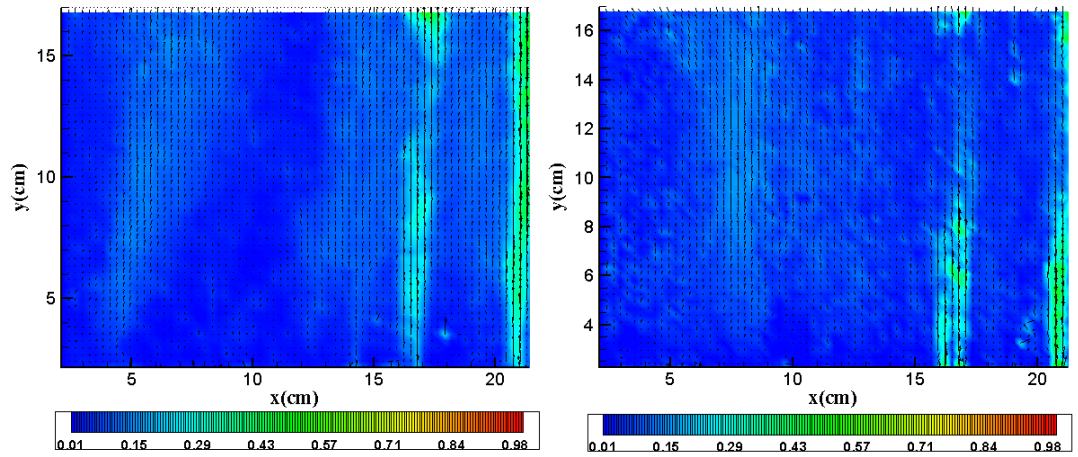

(3) (4)

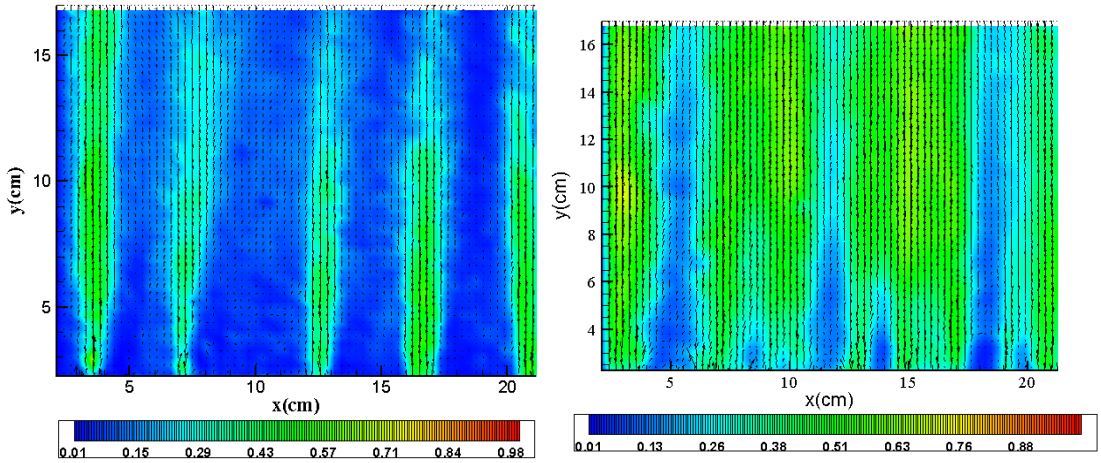

(5) (6)

Figure 21 Contined.

From the PIV analysis result, we can see that, with the increase of wall heat flux, both the nucleation site density and the velocity increase a lot. Driven by the rising bubbles, liquids around the nucleation site and above the nucleation sites tend to have larger velocity. From Figure 21, we can see the bubble jets became more and more obvious and active as the increase of wall heat flux.

The velocity field results are not very satisfactory. The vortex and other characteristics cannot be observed in the above figures. The main reason behind this is that the particle tracers are not suitable for this experimental condition. The density of this kind of silver coated hollow glass spheres is 1.4 g/cm^3, the same with refrigerant. However, when heated, the density of refrigerant decreases, resulting some portion of particle tracers deposited onto the tank bottom. And the remaining particle tracers were not following the fluid motions very closely. Later experiments showed that with lighter particles, e.g. hollow borosilicate glass spheres, the PIV images are more satisfactory. Moreover, in this experiment, the camera was set at a frame rate of 2000 frames/s, which is too high for this low heat flux. From later image processing, I noticed that during single time interval, ΔPIV, the particle tracers barely move. This frame rate was chosen based on previous PIV experiments experience. However, in the past tests, the fluid motion is usually much active than pool boiling condition. This induced very large error in the data analysis. So in later experiments, 500 frames/s is fast enough for the PIV measurements.

Since the working fluid is refrigerant, its boiling point is very low. Thus, the power induced by the laser sheet should be considered in estimating the heat flux onto the pool. When laser is induced into the glass tank, more heat will be induced into the tank. Thus, more bubbles and more nucleation sites are generated. Figure 22 is a snap shot of the same position under same wall heat flux. The left picture without is the laser, while the right one is with laser shining. It is obvious that the laser induce three new

nucleation sites. This effect should be taken into consideration especially under subcooled conditions when wall heat flux is low.

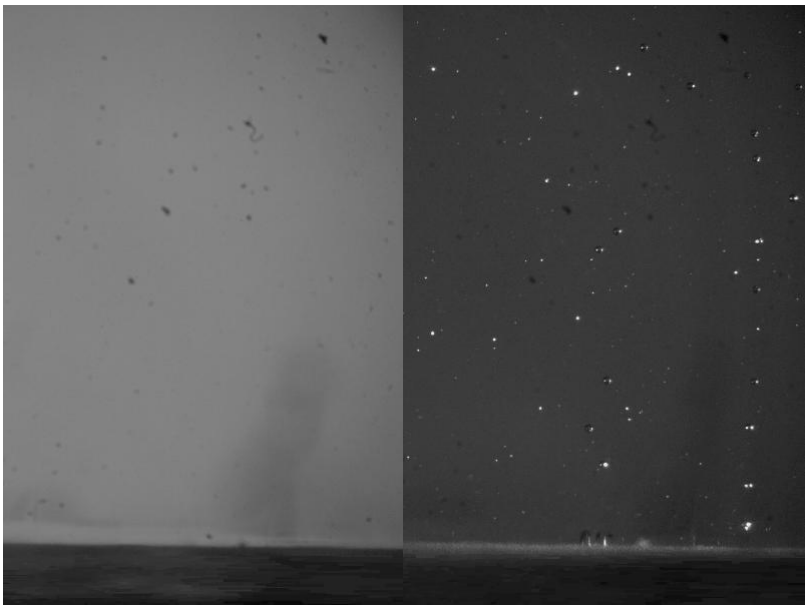

Figure 22 Laser induced heat effects

Moreover, the laser sheet will induce new nucleation sites at a specific heat flux. As shown in Figure 23, the left pictures were taken before the shinning of laser. The right ones are taken after the laser illumination. The red circles label out the newly born nucleation sites. After the shinning of laser sheet, though the laser was turned off, the newly born nucleation sites will remain. This effect is never noticed before. It will have significant impact on PIV and shadowgraphy test results. Usually, people are carrying out PIV and shadowgraphy measurements simultaneously, which means one frame of PIV measurement and one frame of shadowgraphy measurements. In this case, during PIV measurements, the laser sheet will affect the bubble behaviors. Such effect should be taken in to account. It happens at all different heat fluxes, not only one experimental

condition. Figure 23 only shows the experimental condition when heat flux is at 0.11 kW/m^2.

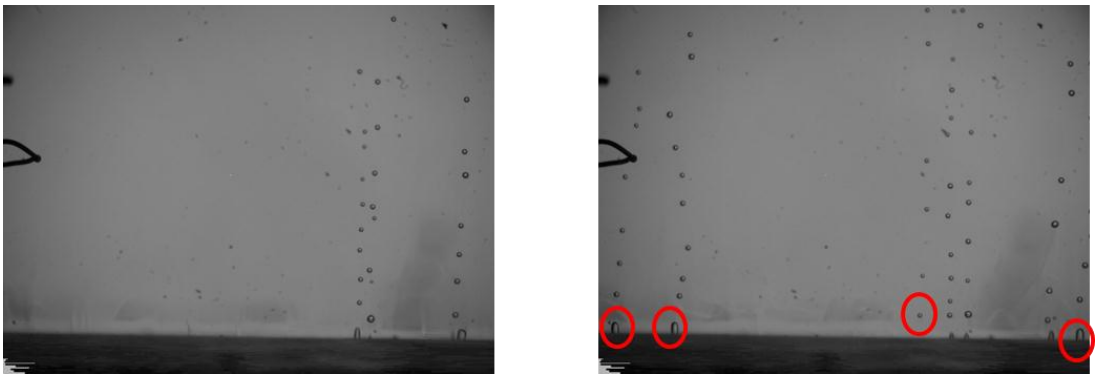

Figure 23 Laser induced new nucleation sites at the wall heat flux of 0.11 kW/m^2

To quantify the amount of heat induced by the laser, and reduce the error of wall heat flux, laser power quantification experiments should be carried out. The laser induced heat flux effect was not noticed only after the pool boiling PIV measurements. This is the first time we noticed such error. In the previous test, either the heat flux is high enough to cover the laser effect, or the working fluid has a much higher boiling point, such as water. Aware of this influence, laser power quantification tests were carried out for the subcooled flow boiling experiments.

From the experiments done by my colleagues, the average energy deposition rate by the laser sheet to the pool of refrigerant is estimated. From the results, we know that the estimated deposition ratio is approximately 0.3164. The heat induced by laser is calculated by

$$Heat\ flux\ induced\ by\ laser = \frac{Total\ power\ from\ laser\ (1W) \times EstimatedDeposition\ Ratio\ (\approx 0.1364)}{Area\ covered\ by\ laser\ sheet}$$

After simple math, it shows that the amount of heat induced by laser sheet is comparable with the wall heat flux. Such quantification tests are necessary.

4.2 Bubble Shadowgraphy Data Process and Results

4.2.1 Data Analysis Process

The image processing software Image J was used in processing of shadowgraphy images. Image J is a Java based imaging processing and analysis software. This software can display, edit, process 8-bit color and grayscale, 16-bit integer and 32-bit floating point images. It can read many image formats including TIFF, PNG, GIF, JPEG, BMP, DICOM, FITS, as well as raw formats. Image J supports image stacks, a series of images that share a single window, and it is multithreaded, so time-consuming operations can be performed in parallel on multi-CPU hardware. Image J can calculate area and pixel value statistics of user-defined selections and intensity threshold objects. It can measure distances and angles. It can create density histograms and line profile plots. It supports standard image processing functions such as logical and arithmetical operations between images, contrast manipulation, convolution, Fourier analysis, sharpening, smoothing, edge detection and median filtering. It does geometric transformations such as scaling, rotation and flips. The program supports any number of images simultaneously, limited only by available memory.[33]

The analysis process of shadowgraphy raw data includes three major steps, as described as follows.

First, videos got from the high speed camera were broken down to raw images, with the windows 8-bit grayscale BMP format. This raw image includes both the

bubbles and background. In the raw image, the background is brighter than the bubble area. Light from the lamp shines onto the test section, the camera captured the bubble shadow area. However, bubble areas are preferred to be the brighter area, for easier image processing. Thus, the raw images were firstly being reverted, as shown in Figure 24. This image processing step was used for every image including the background images. To reduce error from background images, a few background images of the same position were taken. The images shown in Figure 24 are the average of all the background images. In this work, 100 background images were used to obtain the average background. A background image was taken without any heating or boiling.

Then, images with only the bubbles were obtained by subtracting the background images from the raw images. The image becomes bright bubble shapes with black background. This is much easier for future image analysis. The final images become bright bubble with black background. In this way, the only intensity the software detects comes from bubbles. An example of the final images is shown in Figure 24.

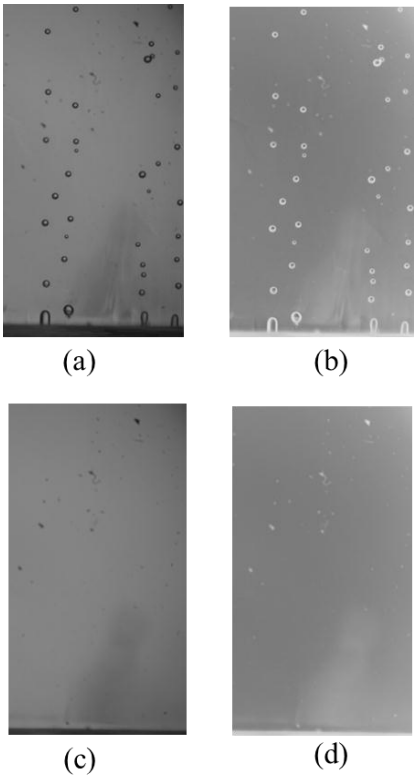

Figure 24 (a) is the original image, (b) is the inverted image. It is similar for (c) and (d), except that (c) and (d) are background images without any boiling happening

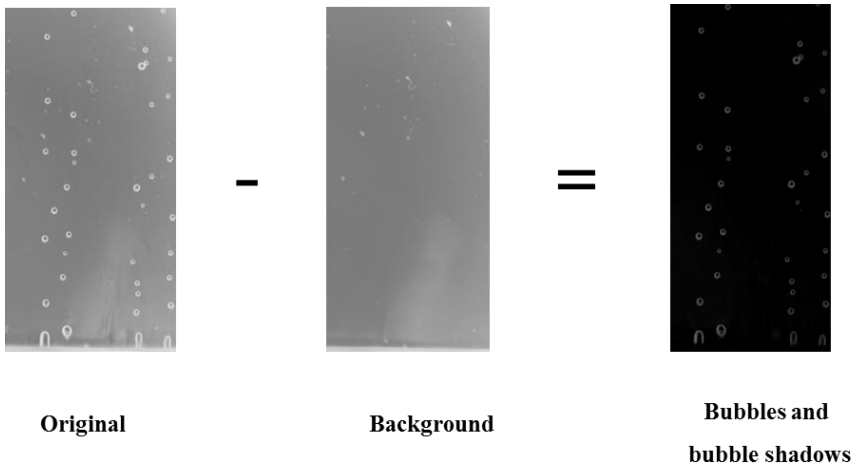

Figure 25 An example of final image, using inverted raw images subtracting inverted background images

Using Image J, an area of interest was defined in the image stack window. Then the area gray scale profiles with respective to time was obtained, shown in Figure 26. From a stack of images, grey scale intensity in the area of interest fluctuates with respect with time. When the bubble passes through the area, the grey scale value will hit a peak. After the bubble passed, its grey scale will decrease to the minimum value. The change of grey scale reflects the bubble generation frequency. Also, from the slope of the rising peaks, bubble growth time and bubble departure time could be roughly estimated.

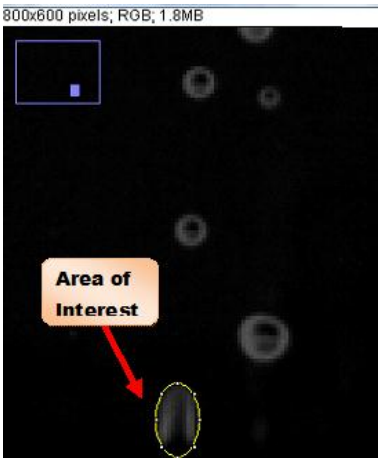

Figure 26 Define area of interest, from which the time=dependent intensity profiles is obtained, which is used as input of later frequency analysis

The intensity profile was used as an input signal of the MATLAB program. Then the time-frequency analysis was carried out. By Fourier analysis, the gray scale profile function of time was converted into a new function of frequency. This function of frequency is also referred to as frequency spectrum of the original grey scale function. By fast Fourier transform (FFT), a dominate frequency could be found from the original signal. After the FFT analysis by MATLAB, a frequency spectrum was obtained, from

which, a dominate frequency can be seen. This dominate frequency is considered to be the bubble departure frequency for the specific nucleation site.

The analysis results from the experiments are introduced below. For each heat flux condition, several nucleation sites were analyzed simultaneously. In total, there are 6 different heat flux measured. And the boiling didn't occur not until the heat flux was increased to 0.062 kW/m^2. Thus in case of shadowgraphy analysis, only the latter 4 heat flux is considered important for bubble dynamics parameters. Figure 28 shows the bubble departure frequency with respect to wall heat flux.

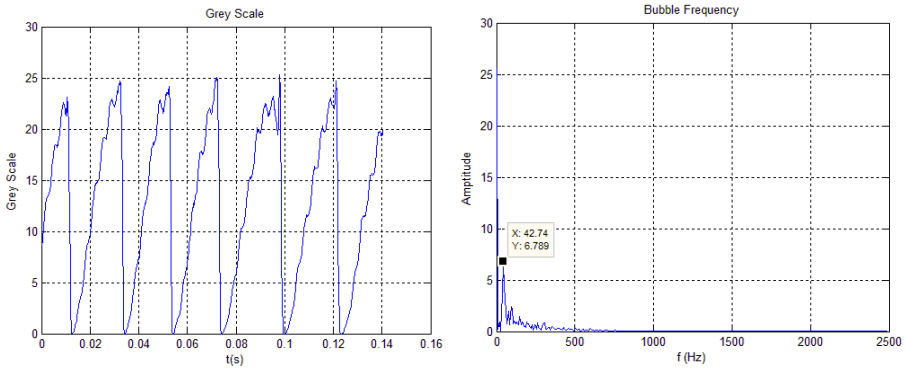

(a) q''=0.06217 kW/m^2 I =0.20 A, V=13.1 V

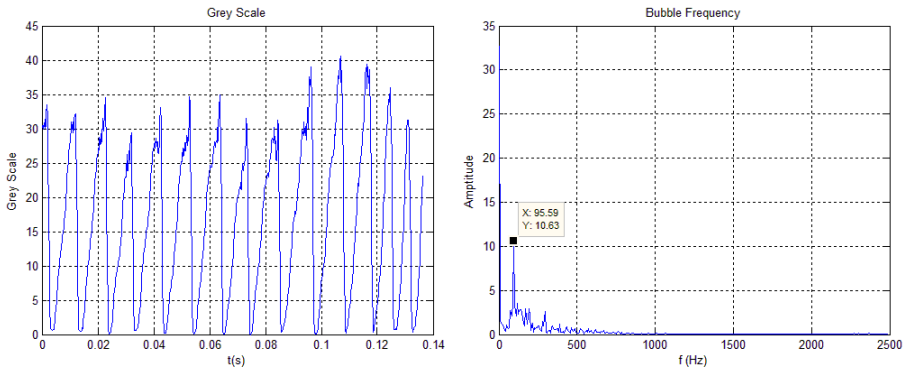

(b) q''=0.1104 kW/m^2 I =0.25 A, V=16.1 V

Figure 27 Bubble departure frequency results from shadowgraphy experiments with different heat flux

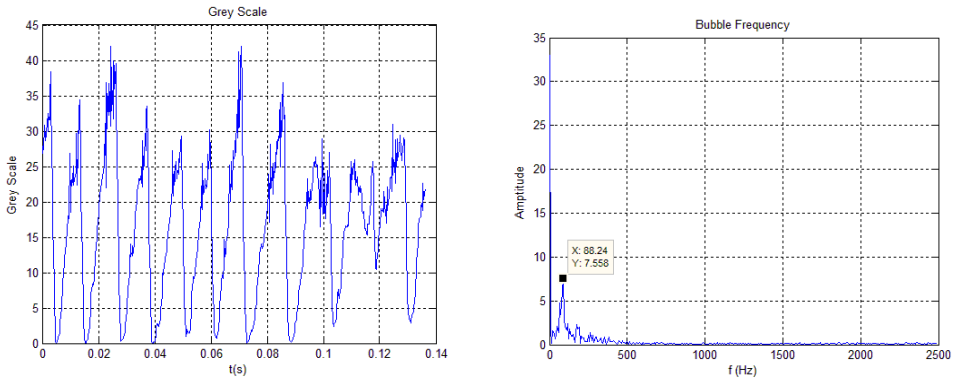

(c) q''=0.166 kW/m^2 I =0.30 A, V=19.1 V

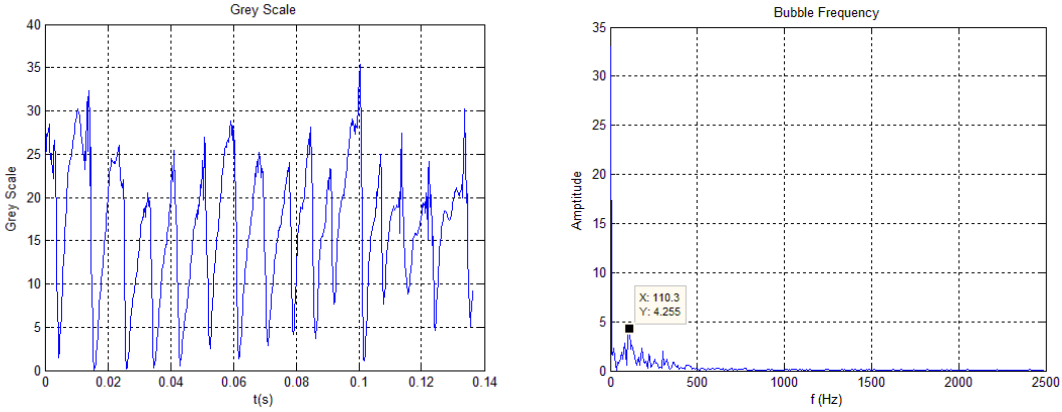

(d) q''=0.2665 kW/m^2 I =0.35 A, V=22.7 V

Figure 27 Continued.

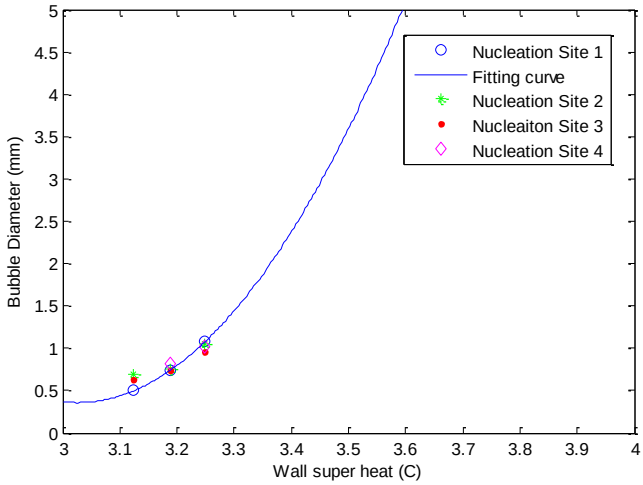

Figure 28 Bubble departure frequency vs. wall heat flux

Similar to the analysis of bubble departure frequency, the dimension of the same area of interest could be obtained at the same time with the intensity profile. The bubble covered area can be measured in pixels. With the known converting factor, the bubble actual size can be estimated. For each heat flux condition, several nucleation sites are tracked. The bubble departure diameter change with respect to wall heat flux is shown in Figure 29.

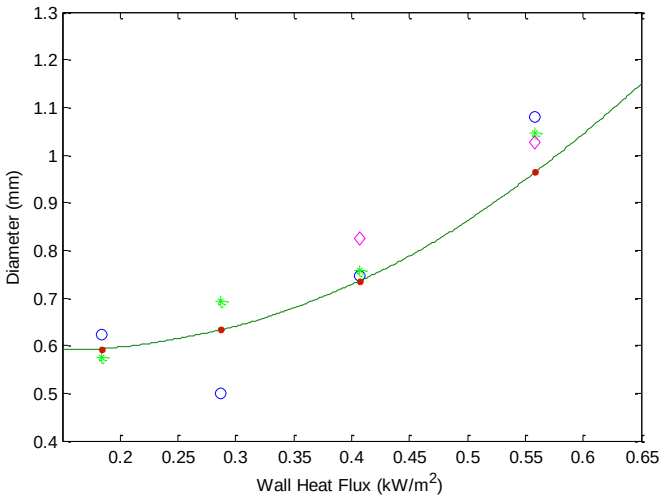

Figure 29 Bubble departure diameter vs. wall heat flux

4.2.2 Results Discussion

In previous research about pool boiling bubble dynamics, bubble departure diameters are assumed be influenced by the net force acting on the bubble, basically the buoyancy force and the surface tension. Some people will take into account the shear force induced by other neighboring bubbles. In the upward facing heater, buoyancy force tends to pull the bubbles up, away from the heater. The surface tension is crucial during the bubble growth period. Besides net forces, heater wall heat flux, wall super heat, nucleation sites cavity characteristics and thermophysical properties of the fluids will also influence the bubble departure diameter.

Craig Geradi [34] concluded several empirical experimental bubble departure diameter results using water as working fluids. Most of these empirical correlations relate the bubble departure diameter with wall super heat. The trend lines are shown in

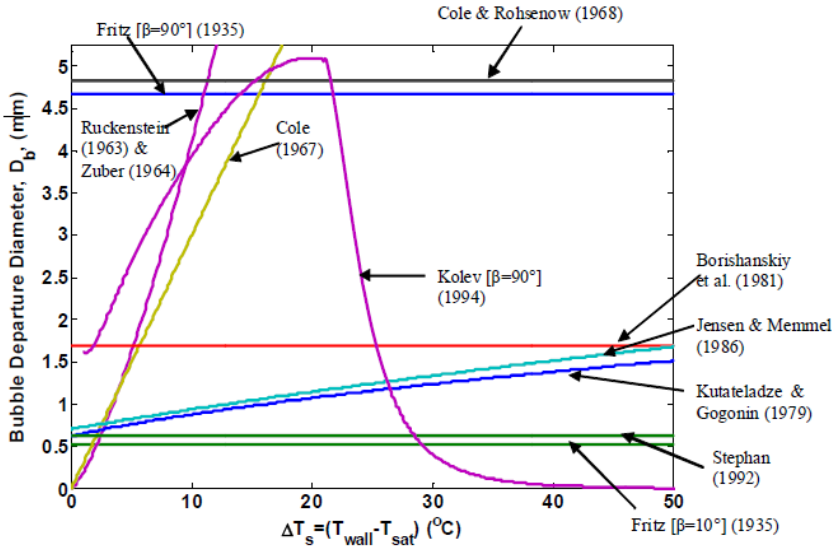

Figure 30 Bubble departure diameter v.s. wall super heat by previous experimental correlations, concluded by Craig Geradi [34]

By comparing these empirical models with my own experimental data, we found that the experimental data fits the Ruckenstein model[6] the best. In this model, besides the buoyancy forces and surface tension force, the shear forces induced by departure of neighboring bubbles are also considered. The bubble departure diameter was related with Jakob number, Ja. Ja is a non-dimensional number widely used in describing the phase transition phenomena. The correlation is expressed in Equation (19).

$$D_b = \left(\frac{3\pi^2 \rho_l \alpha^2 \, g^{1/2}(\rho_l-\rho_v)^{1/2}}{\sigma^{3/2}}\right)^{1/3} Ja^{4/3} \left[\frac{\sigma}{g(\rho_l-\rho_v)}\right]^{1/2} \quad (19)$$

As in many articles, the bubble departure frequency is normally defined as the reciprocal of cycle timet_{cycle}. Here t_{cycle} is the sum of the growth time, t_g and the wait time t_w.[35]

$$f_d = {}^{1}/_{(t_w + t_g)} \quad (20)$$

Waiting time depends on the temperature field in both the solids and the liquid in vicinity of the nucleation site. Growth time depends on the bubble and its departure diameter. It is very difficult to develop a model to predict the bubble departure frequency. It is associated with bubble diameter and wait time, growth time. The latter parameters are affected by the temperature field in two phase flow. Usually, it is assumed that bubble departure time is small enough compared to bubble growth time, so t_w is neglected.

In this way, it is acknowledged that bubble departure frequency is determined by the bubble departure diameters. However, the departure frequency varies from nucleation sites to nucleation sites. A mean bubble departure frequency was usually estimated at given wall heat flux or wall super heat. Craig Geradi [34] concluded several empirical experimental bubble departure frequency results in Figure 31. Zuber's expression in 1959 is the most commonly used one. [36]

$$fD_d = 0.59[\frac{\sigma g(\rho_l - \rho_v)}{\rho_l^2}]^{1/4} \quad (21)$$

After comparing my experimental data with previous models, it is found that the frequency v.s. diameter trends fit the Zuber correlation the best. However, there are noticeable discrepancy between experimental data and previous empirical modesl. The main reason behind this is that, these correlations are only valid for limited range of experimental conditions, most ly in the saturation boiling rage. For example, Zuber correlation stands between the heat flux range of 8000 kCal/hr/m^2 to 10000 kCal/hr/m^2, which is way above the wall heat flux in this work.

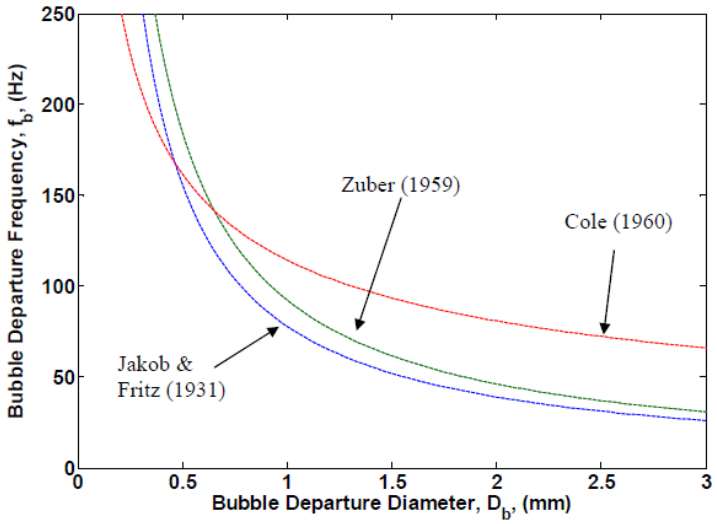

Figure 31 Previous pool boiling experiments data conclusion by Craig Geradi [34]

4.3 Infrared Measurement Results Analysis

In this work, a FLIR system SC8200 IR camera was used in an attempt to capture the temperature fluctuations of the ITO heater surface in pool boiling. From previous shadowgraphy tests before final experiments, the bubble departure frequency is around 100 Hz. So the temperature fluctuations on the heating surface should around this level. The camera was set at a frame rate of 131.5 Hz with a spatial resolution of 1024 × 1024. Measurements were taken under the latter three experimental conditions from Table 1.

Validation experiments had been carried out by my colleagues, proving that the infrared camera could catch up with the frequency change in the experiments. The small tests were taken by setting the infrared camera in front of a copper plate. Laser beam was used as heat source with certain frequency. By analyzing the images from IR camera, intensity fluctuations were obtained. After the time-frequency analysis, it is found that, the IR camera could capture the temperature change with a frequency up to 100 Hz. In

this way, it is believed that the temperature fluctuation on the heating wall should be captured by the IR camera. Efforts were tried to make to identify the frequency from the infrared images, which can be compared to the shadowgaphy results.

Similar with shadowgraphy images, Image J was used for analysis. In the beginning, the video clip was broken down to pictures. Then an area of interest was defined, mainly to cover a little more than the area of nucleation sites. A time dependent intensity profile is then obtained, shown in Figure 32. This is under the heat flux of 0.11 kW/m^2. After time-frequency analysis, dominate frequency is around 25 Hz. Comparing with bubble departure frequency from shadowgraphy measurement, which is 88 Hz, there is a large difference.

There are several reasons why the infrared camera cannot catch up with the temperature fluctuation on the heating surface. The major reason is that, in this pool boiling facility, borosilicate glass was used as heater substrate. For one thing, temperature change information from the inner surface will have a time delay when transferring through the glass. For another thing, the glass is not transparent to IR lights. This is the main reason why the image itself is not clear enough. There has been similar effort made by other researchers, using infrared camera synchronized with high speed shadowgraphy to study the bubble dynamics in pool boiling [37]. ITO coated sapphire glass was used as heater. Temperature fluctuations of nucleation sites on the wall were presented.

Moreover, it is difficult to obtain the frequency is that the refrigerant bubbles move quite a lot around the nucleation site. Since the infrared images processing method

is based on the greyscale analysis of the image, the movements of bubbles largely increase the uncertainty. Different from refrigerant bubbles, water bubbles tend to stick to the nucleation sites, which makes infrared recording possible. Thus, for future advice, sapphire glass is preferred for IR thermometry.

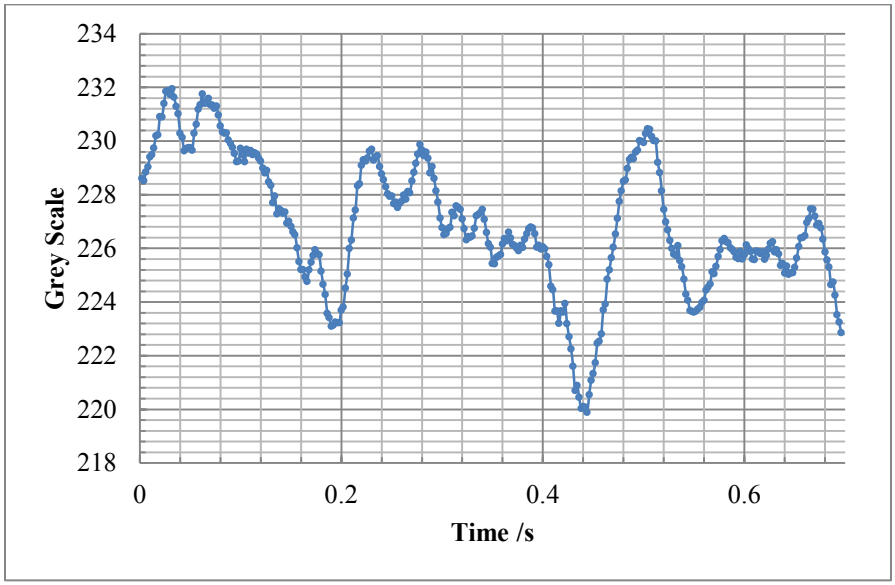

Figure 32 Grey scale profile from infrared images

Though the estimation of bubble departure frequency from wall temperature fluctuations is not successful, the average wall temperature could be estimated through IR images. Using Image J, the average overheats under three different heat flux are concluded in the table below. T_{IR} is the measured value from IR images, while T_{actual} is the actual ITO surface temperature estimated from Equation (16).

Table 2 Wall overheat under different heat flux

Current (A)	Voltage(V)	Power(W)	q''_{total} (kW/m^2)	T_{bulk} (K)	T_{in} (K)	T_{actual} (K)	T_{IR} (K)	ΔT(K)
0.25	16.3	4.075	0.28	296.25	317.85	318.21	320.65	0.36
0.30	19.3	5.79	0.41	296.75	324.35	324.95	327.95	0.60
0.35	22.7	7.945	0.56	297.55	329.45	331.14	334.65	1.69

In the infrared measurement, the IR camera was place right below the heater; nucleation site density could be identified from infrared images. Each temperature fluctuating point in the infrared images correspond to one nucleation site. Thus, nucleation site density can be estimated in Figure 33.

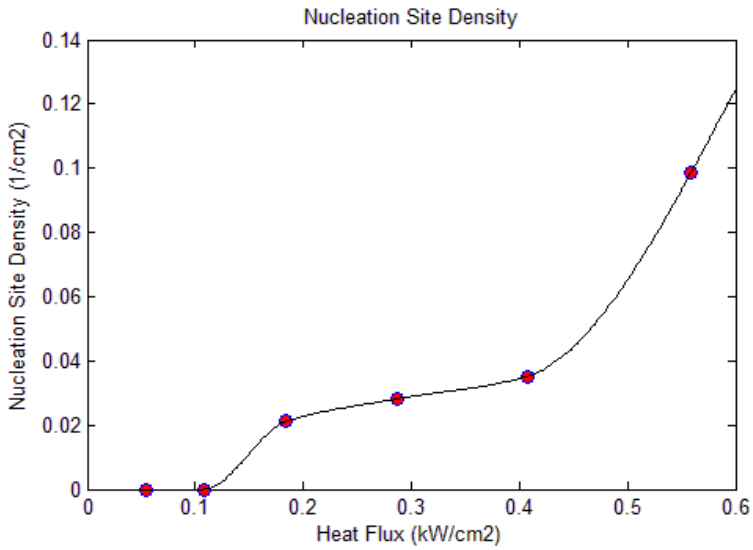

Figure 33 Nucleation sites density vs. wall heat flux

5. RICM MEASUREMENT AND IMAGE PROCESSING

In this section, the RICM measurements test was discussed. The test facility was explained. Using the principle from previous section, the methods of image processing (absolute surface height and shape reconstruction) are discussed in detail. At last, the preliminary test results are introduced.

5.1 RICM Test Facility

As shown in Figure 34, the RICM pool boiling facility set up consists of a bottle with thin ITO heater on the bottom. The cover glass is borosilicate glass with the dimension of 18 mm × 18 mm × 0.1524 mm. The ITO layer is 12 ohms/square. The ITO heater surface was etched to the following pattern in order to make sure the hot spots are in the center area of view. Thus, the potential nucleation sites might appear in the center. Such pattern proved successful in the pool boiling experiments. In the graph below, the slash shaded area is the remaining ITO strip. Conductive silver paint was applied at the corner area of the ITO pattern, so as to connect to the copper wires which can be connected to DC power supply. The conductive silver paint is the same type as used in the previous pool boiling heater setup. The red spots in the center are potential spots which nucleation sites might occur. Figure 35 is the RICM facility photo look. Refrigerant was used as working fluid because of its low boiling point.

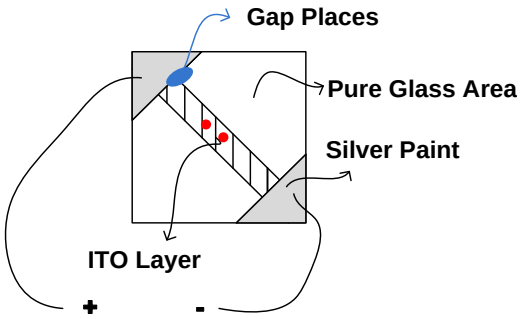

Figure 34 ITO heater schematic drawing

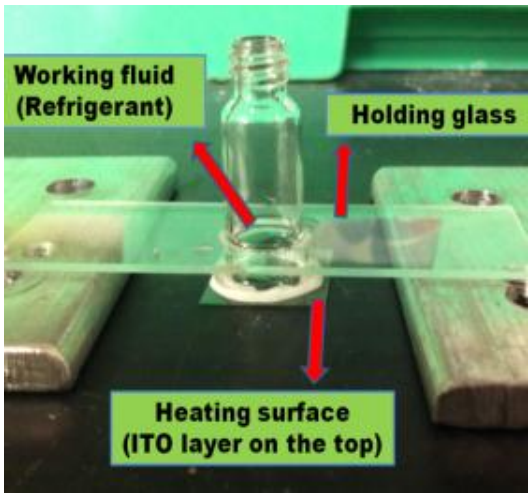

Figure 35 RICM facility close look

The experimental RICM setup that facilitated image acquisition consisted of a Zeiss Axiovert 200M inverted microscope with a 103W HBO mercury vapor lamp coupled to a Zeiss AxioCam MRm camera; a 5nm band-pass filter used to obtain the monochromatic green light, 546:1 nm; and a Zeiss Antiflex EC Plan-Neofluar 63x=1:25 Oil Ph3 objective.[26]The microscope and the experimental facility are shown in Figure 36.

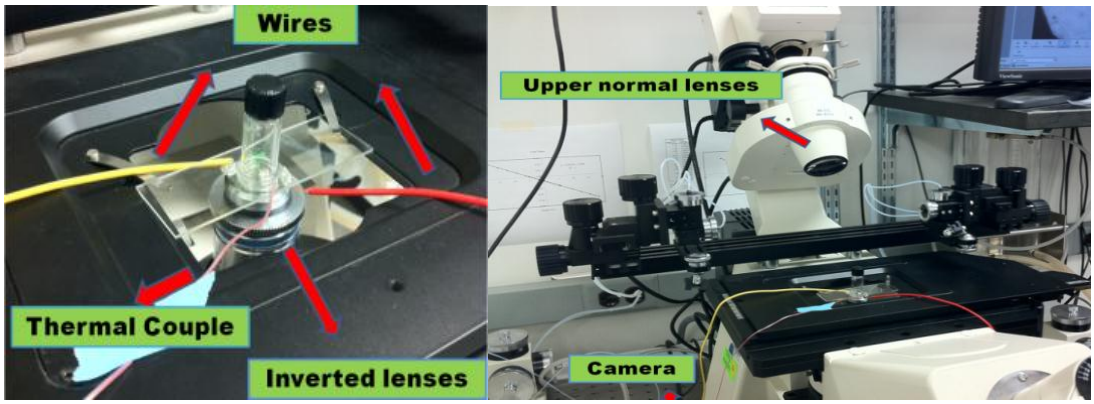

Figure 36 RICM experiments setup

5.2 Image Process and Height/Shape Reconstruction

The relation between surface height at various lateral positions and RICM image intensity had been discussed in the previous sections. As shown in Figure 37, from the RICM images, we could obtain the intensity profile with respect to positions. Then, after surface reconstruction, the surface height along with surface contact angles can be estimated. In this section, two surface reconstruction methods are introduced.[18]

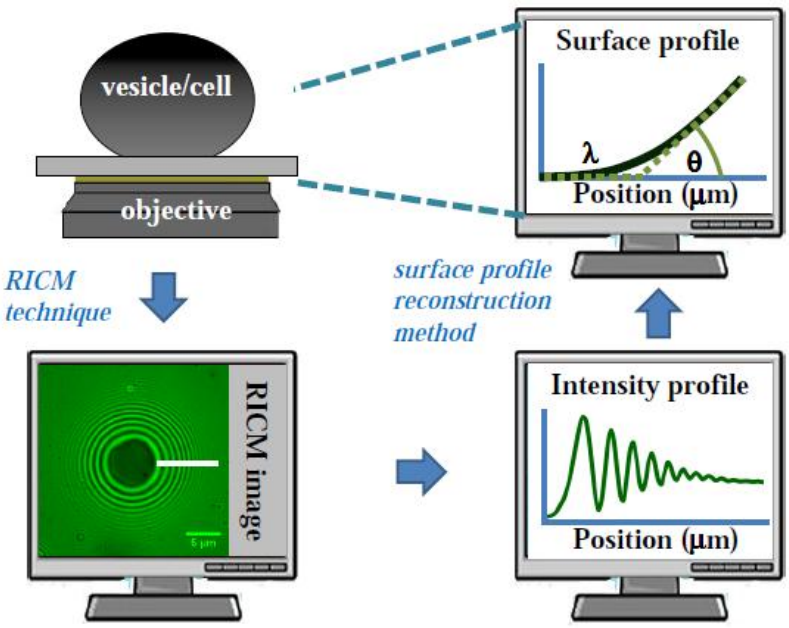

Figure 37 RICM image processing procedure[26]

5.2.1 Min/Max Method

For a planar interface, experimental maximum and minimum intensities, directly obtained from the images can be assumed equal to the theoretical values in the theoretical relation. In this case, the interface distance h can be calculated by the following equation.

$$\frac{2I-(I_{max}+I_{min})}{I_{max}-I_{min}} = cos(4\pi n\frac{h}{\lambda}) \quad (22)$$

Here, n is the refractive index of fluid and λ is the wavelength of incident monocratic light rays.

For partially adherent particles, the adhered part was assumed to be the first branch. As the surface height increases continuously, subsequent integers can be assigned to fringes accordingly and choose the correct branch.

This method holds when the noise due to scattering from surface defects is not significant enough to dominate the maximum and minimum intensities extracted from experimental data. Another important precondition for this method to hold is that INA is small. Moreover, if reflection from multiple interfaces is important, this method is only valid for obtaining the relative height instead of absolute height. Under such scenario, a different method was introduced.

5.2.2 The Refractive Index Method

When multiple interfaces interference is considered, the fringes will shift by a distance of h_0 comparing to the original fringes. Thus, when reflection from multiple interfaces cannot be neglected, the Min/Max method is no longer valid. In this case, if refractive index is known, the objective/substrate surface distance can still be determined. This method is illustrated when considering a three interfaces scenario shown in Figure 38.

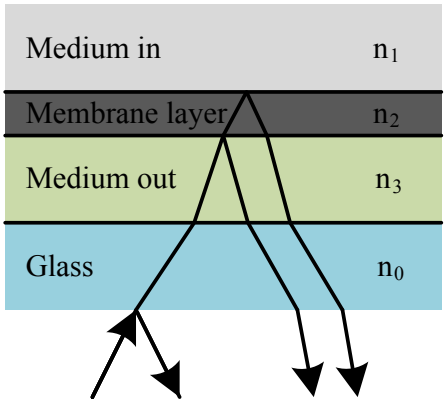

Figure 38 Triple interface interference

In this method, firstly, the theoretically expected intensity is generated by Equation (24)

$$2I = S - 2Dcos\{2k[h(x,y) - h_0]\} \tag{23}$$

Where $h_0 = -\frac{\lambda}{4\pi n_{out}} arctan\frac{\gamma sin\delta}{1+sin\delta}$, $\gamma = \frac{r_{23}}{r_{12}}(1 - r_{12}^2)$ and $\delta = 4\pi n_m {}^{d_m}/_{\lambda}$.

Then the intensity is normalized with respect toI_0. By inverting Equation…, distance can be estimated.

$$\frac{I_{th}-I_0}{I_0} = Y_0 - R_0 cos(4\pi n\frac{h-h_0}{\lambda}) \tag{24}$$

Here Y_0, R_0 and h_0 are constants related to the refractive index of the medium. The refractive index is modified by

$$r = r_{01} + (1 - r_{01}^2)e^{4\pi i n_1 d_1/\lambda}[r_{12} + r_{23}(1 - r_{12}^2)e^{4\pi i n_{2d_2}/\lambda}] \tag{25}$$

In the following sections, the surface reconstruction methods are introduced.

5.3 Height Reconstruction with Known Symmetric Shape

In case of pool boiling experiments, we would like to obtain visual access of microlayer between bubbles and heating surface. It is assumed that before the attachment of bubbles from heating surface, the bubbles shapes are spherical. Therefore the resultant fringes were supposed to be circular symmetry. The interference image consists of an array of concentric circular fringes. Height increment between object/substrate surfaces will change the fringe patterns in a symmetric way.

From previous theories, we can deduce the relation between the heights between the surfaces. The correlation between the height h and the radius position r_l of the l^{th} interference fringes is expressed in the following equation.

$$h(r_l) = \frac{\lambda l}{2n} - R + \sqrt{R^2 - r_l^2} \tag{26}$$

The expression needs further improvement, since it didn't take account of the illumination aperture and the object curvature. This method does not depend on the models. However, it depends on the microscope. Such method is robust, but it has the limitation of the mono-wavelength RICM. To determine he absolute height, the dual-wave approach has to be adopted. [18]

In practice, the quality of data obtained from the green wavelength is superior to that obtained from the blue light. Since the green line of mercury is stronger than blue and the quarter-wave plate is optimized for green. [18]

There is a simple planar surface reconstruction method. In this model, the surface to surface height increment is constant along the radial direction. Δh is related with the distance Δx between two adjacent intensity extremes, expressed in the following equation.

$$\Delta h \cong \frac{\lambda}{4n_1} \tag{27}$$

For more accuracy, there is an improvement based on simplified non-planar model. Considering the relation between the height increment and the surface slope, the following equations were made.

$$\left[\frac{h(x_{i+1})}{1-(tan(\beta_{i+1}))^2}\right] - \left[\frac{h(x_i)}{1-(tan(\beta_i))^2}\right] = \frac{\lambda}{4n_1} = \Delta h_{planar} \tag{28}$$

$$tan(\beta_i) = \frac{\Delta x_i}{2\Delta h_{planar}} - \sqrt{\left[\frac{\Delta x_i}{2\Delta h_{planar}}\right]^2 - 1} \tag{29}$$

In this work, a simplified non-planar model was used for surface reconstruction. As we know, in the planar model, the height increment between fringes is constant, as in Equation (31).

$$\Delta S^p = \lambda/4n_{liquid} \tag{30}$$

However, in the planar model, the curvature of the surface is not considered. If considering surface curvature, the position on fringes doesn't reflect the information of surface. Instead, from the position xf on the fringes pictures, we can obtains the surface height at xb. This principle is shown in Figure 39. Point B on the fringes contains the surface information of Point β. The relation of xf and xb is expressed in Equation (32) to (34).

$$\Delta x_f^j = \frac{\Delta S^p}{sin(\beta^j)} \tag{31}$$

$$\Delta S^j = \Delta S^p cos(\beta^j) \tag{32}$$

$$\Delta x_\beta^j = \Delta x_f^j - \Delta S^j tan(\beta^j) \tag{33}$$

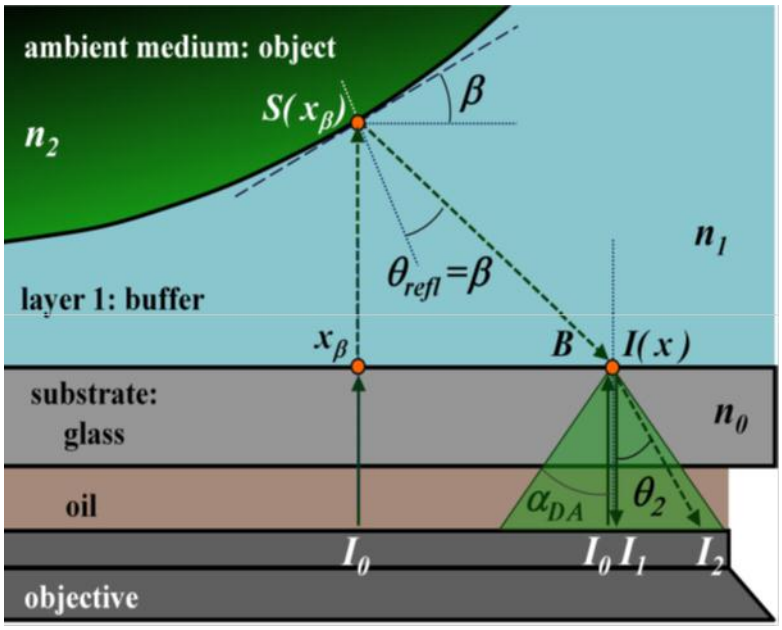

Figure 39 RICM Surface reconstruction principle scheme[26]

Assuming the first fringe on the RICM pictures is the actual first fringe formed. We can calculate the starting point of surface height increment.

$$S\left(x_\beta^1\right) = \Delta S^p cos(\beta^1) \tag{34}$$

$$x_\beta^1 = x_f^1 - S\left(x_\beta^1\right) tan(\beta^1) \tag{35}$$

5.4 RICM Images Results and Discussion

Since RICM techniques is originally developed to characterize micropaticles, there is doubt that whether this techniques can be used in two phase flow field for bubble dynamics. Some pre-measurement tests were carried out to prove the possibility of this technique. Figure 40 shows the microscopic view of the heater under inverted microscope. The picture on the left shows the nucleation site without heating. From the

photo, we could see that there is a crack on the surface of the ITO heater. Nucleation site was formed along the crack. The one on the right was taken under boiling. Heat flux was kept at very low level, so that there is only one nucleation site in the view, and only one bubble generates at a time. Fringes from the bubbles could be easily seen. From this image, RICM techniques were proved possible to obtain the bubble dynamics parameters.

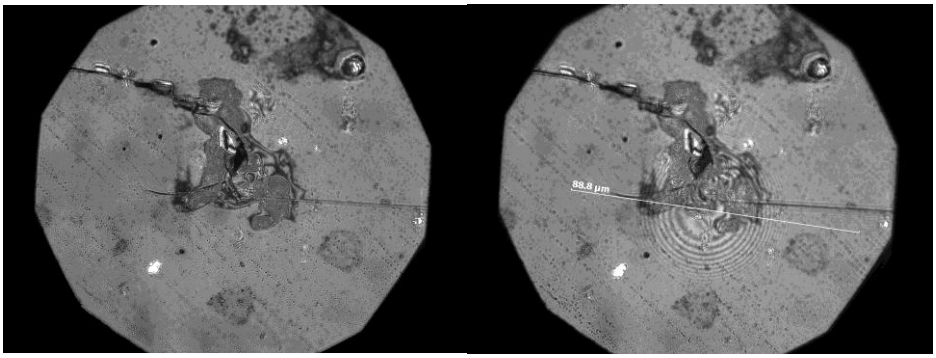

Figure 40 Background picture of nucleation site

After proving the possibility of RICM technique, some image processing efforts were made in an attempt to obtain the bubble diameters and the bubble-surface sublayer thickness. The bubble was assumed to be in spherical shape. Image J was used for image processing. First, a center point was defined. Then, intensity profile along the radial direction was measured, as shown in Figure 41.

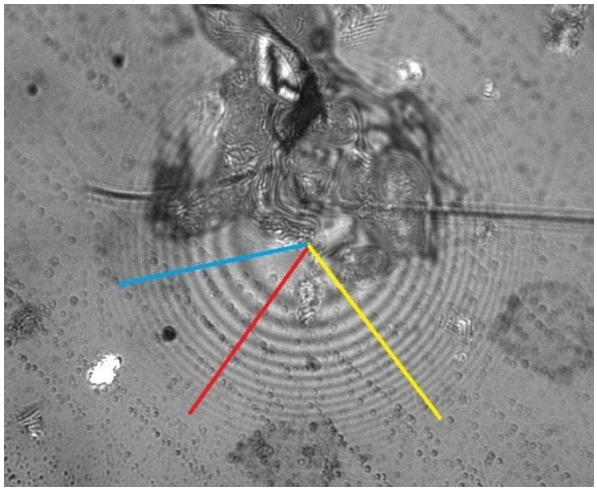

(a)

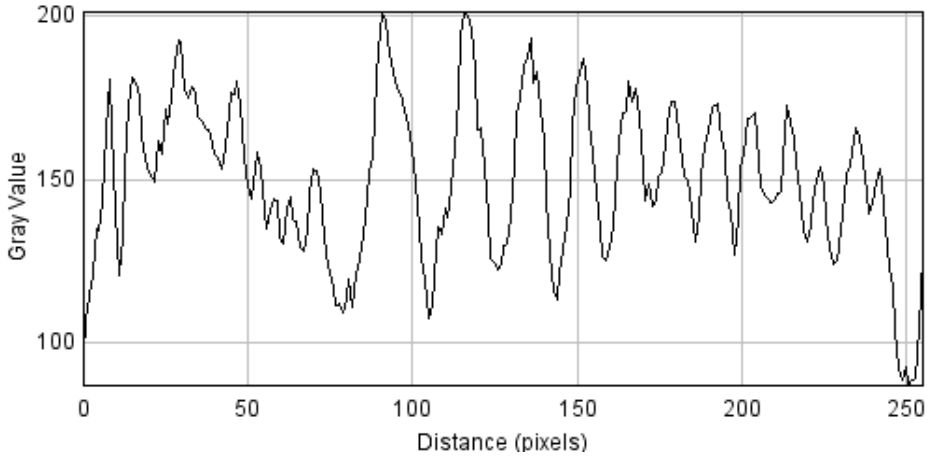

(b)

Figure 41 (a) is the intensity analysis process. (b) is the intensity profile in radial direction

Based on the radial intensity profile, bubble surface reconstruction could be carried out. Basic analysis principles are discussed in the previous section. From spacing of adjacent fringes, bubble surface to glass surface height can be estimated. Before quantification, calibration of RICM images was carried out. From the calibration results,

we know that on the image, 88.8 μm length lines equals to 867 pixels. Thus the conversion factor is 0.1024 μm/pixel. In this way, the intensity profile with respect to radial spatial distance is plotted.

Bubble-surface contact angles and the thickness of micro-layer can be obtained by analyzing the interference fringe patterns. From the distance between adjacent fringes, the surface height could be determined. As in this model, the spatial distance between the intensity extremes is measured in Image J, as shown in Figure 41. To avoid error, three measurements were taken. As shown in Figure 41 (a), define the center as the starting point, the grey scale profiles were obtained along three different lines. The minimum grey scale points represent the positions of fringes.

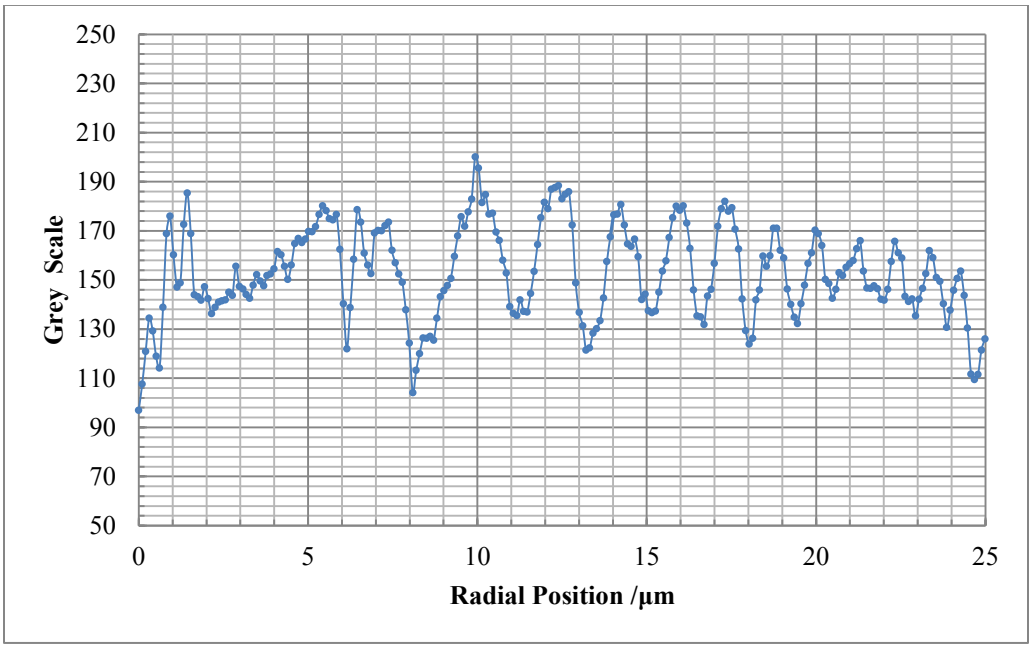

Figure 42 Grey scale profiles in radial direction, 3 measurements

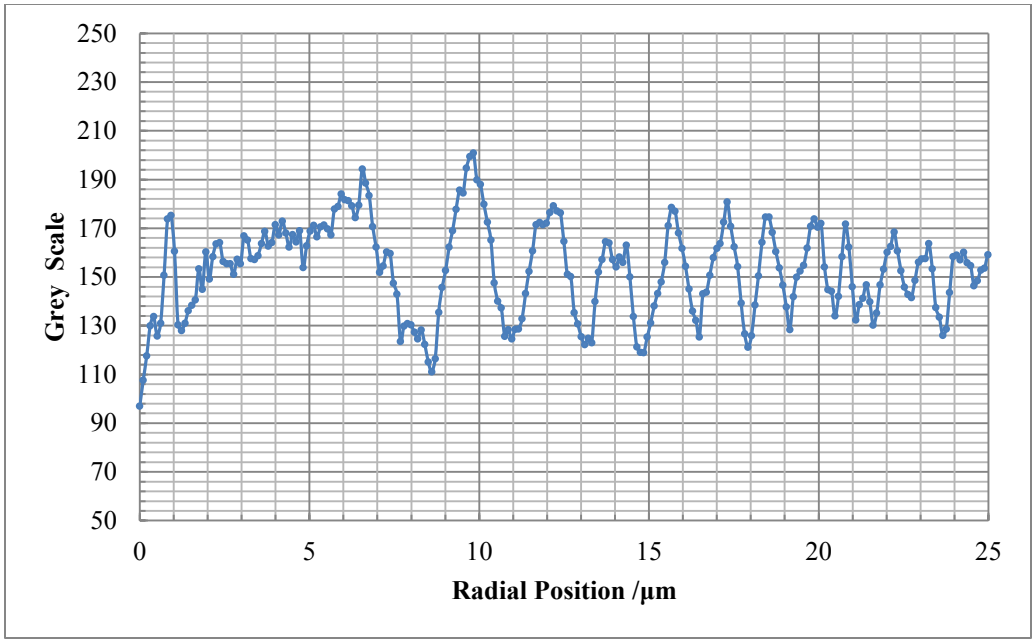

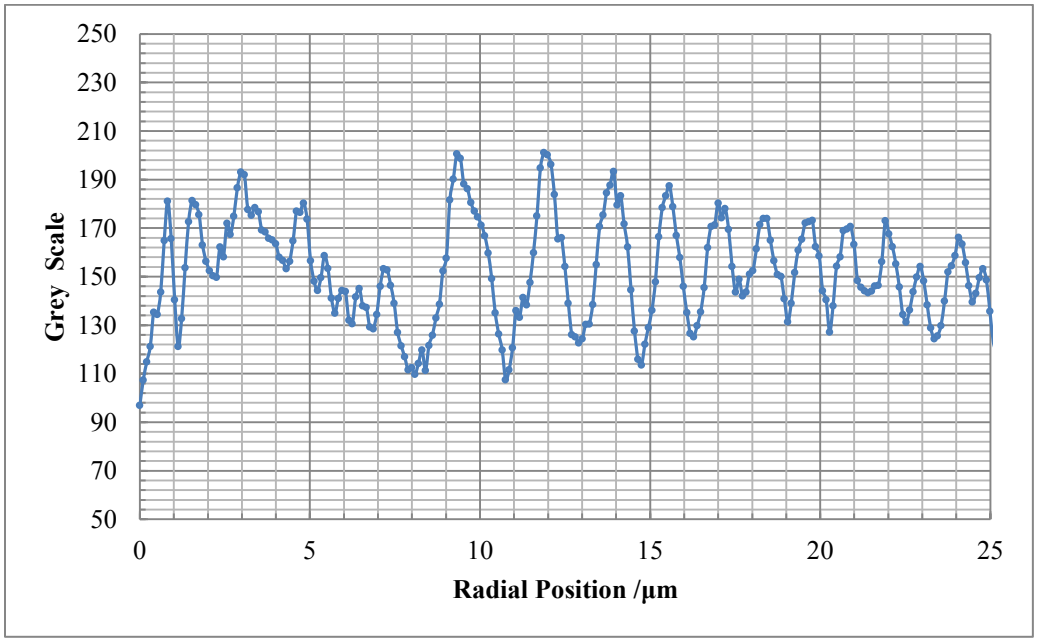

Figure 42 Continued.

From the gray scale profiles, the distance between adjacent intensity extremas were obtained, as in Figure 43. To achieve better accuracy, the fitting equation was used

to calculate the distance between two adjacent extremas on fringes. The data was listed in Table 3.

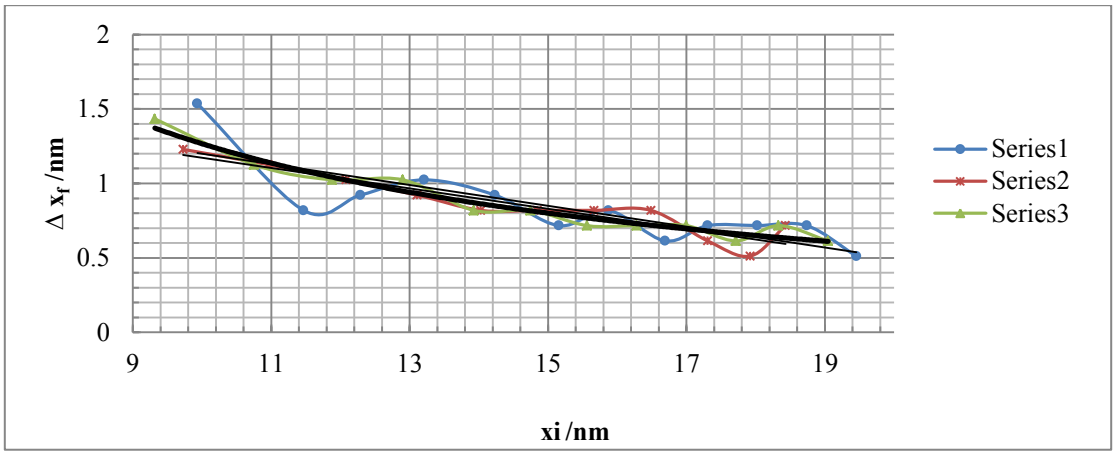

Figure 43 Distance between adjacent extrema on the RICM image fringe patterns

Table 3 Distance between two adjacent extremas on fringes

Number of fringes	1	2	3	4	5	6	7	8
x_i /nm	8362.667	11059.2	13073.07	14916.27	16486.4	17885.87	19217.07	20497.07
Δx_f /nm	1550.145	1129.722	934.8186	805.1622	718.9194	655.5795	604.4117	561.8646

Using the simplified non-planar model, which is discussed in detail in previous section, surface reconstruction was carried out. The surface height increments, contact angles were listed in Table 4.

Table 4 Surface reconstruction parameters

Number of fringes	1	2	3	4	5	6	7	8
x_i /nm	8362.667	11059.2	13073.07	14916.27	16486.4	17885.87	19217.07	20497.07
Δx_f /nm	1550.145	1129.722	934.8186	805.1622	718.9194	655.5795	604.4117	561.8646
β_j	0.070067	0.096212	0.116355	0.135199	0.151536	0.166307	0.180535	0.194374
Δx_β^j /nm	1542.547	1119.296	922.2196	790.5344	702.5368	637.6141	584.9254	540.9026
ΔS^j /nm	108.2591	108.0235	107.7916	107.5351	107.2818	107.0281	106.7617	106.4818

Assuming the first fringe from the RICM image was the actual first fringe formed. The starting point of RICM surface reconstruction was carried out. The actual surface heights at different positions were listed in

Table **5**. Assume that the new born bubble is in spherical shape. Using MATLAB to fit a circle curve, Figure 44and Figure 45 was obtained.

Table 5 Surface height increments v.s. radial positions

	1	2	3	4	5
x_β^j /nm	8355.069	9897.616	11016.91	11939.13	12729.67
S^j /nm	108.2951	216.5183	324.5418	432.3335	539.8686
	6	7	8	9	
x_β^j /nm	13432.20	14069.82	14654.74	15195.65	
S^j /nm	647.1503	754.1784	860.9401	967.4219	

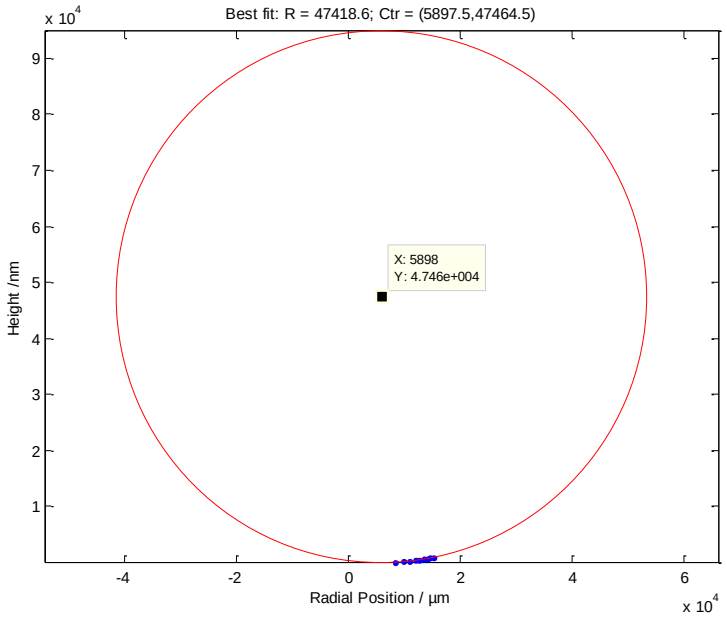

Figure 44 Bubble Surface Reconstruction

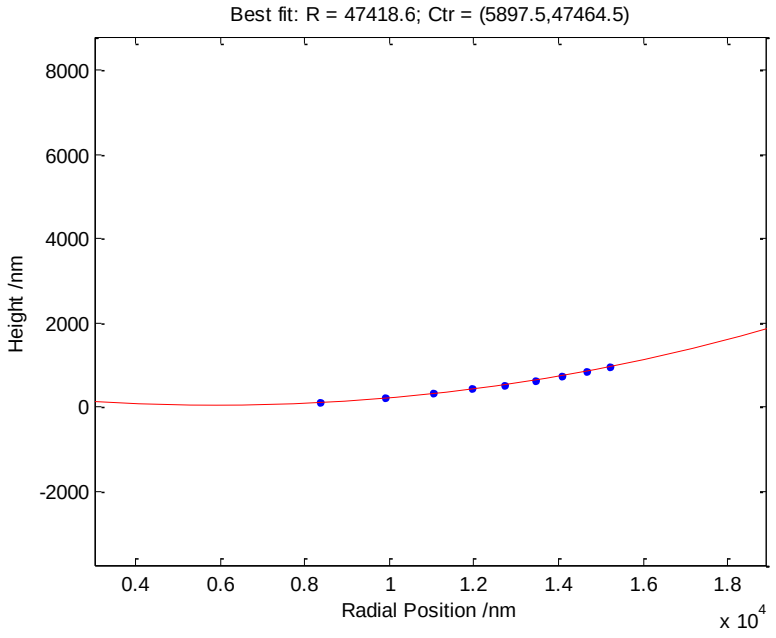

Figure 45 Fitting curve enlargement view

To conclude, this new technique can be used in measuring the pool boiling phenomena. However, the fabrication techniques of ITO heater should be improved. The hot spot, or the potential nucleation sites are preferred to be located in the center of microscope view. However, if the pattern in Figure 34was used, nucleation sites are normally firstly happen along the edge of the silver paint. After detailed observation from the microscope, it is found that there is a gap between the silver pain layer and the ITO glass. The silver paint or silver cannot attach to the glass surface perfectly. In this way, a very trivial amount of refrigerant will get in between the gap. When heated, the trapped small amount of refrigerant will firstly boil. And the first bubble will occur along the silver paint edge. Such kind of bubbles cannot be observed by the inverted microscope. Thus, in the future, if more detailed application are desired, heater fabrication should be improved, for better generation of artificial nucleation sites.

6. CONCLUSIONS

6.1 Summary

The work mainly focused on using various flow visualization techniques to measure the two phase flow parameter in pool boiling experiment. HFE-7000 was chosen as working fluid, mainly because of its low boiling points. PIV was used to measure liquid velocities, while shadowgraphy was used as supplement to obtain bubble dynamic parameters. Infrared thermometry was introduced to depict the pool boiling phenomena from a new aspect, for example, trying to relate temperature fluctuations at nucleation sites with bubble departure frequency. Wall heat flux was set as experimental variable. Six different experiment conditions with increasing heat flux were studied.

Moreover, a new technique RICM was firstly used in an attempt to get more information from a much more micro scale. Based on optical principles, this method has high accuracy inherently.

Experimental results were compared with previous empirical correlations.

6.2 Lessons Learned

From the whole experiments process and later data analysis, valuable experience had been learned. The set up experience of this pool boiling facility greatly benefits other experiments of CASL project. For example, the ITO heater fabrication method was used later in the flow boiling facility. Secondly, a lot of new issues were noticed from the results analysis. For example, laser power induced heat flux is not negligible in both pool boiling and flow boiling experiments. Some new equipment was firstly being used,

such as the infrared camera and microscope. Great efforts were spent on how to understand the infrared camera and its calibration process.

REFERENCES

[1]. M. Corradini, http://wins.engr.wisc.edu/teaching/mpfBook/node26.html,2012.

[2]. S. Nukiyama, The maximum and minimum values of heat Q transmitted from metal to boiling water under atmospheric pressure, in J. Jap. Soc. Mech. Eng. 1934. p. 367-374.

[3]. G. Kocamustafaogullari, M. Ishii, Interfacial area and nucleation site density in boiling systems. Int. J. Heat Mass Transfer, 1983. 26:670-679.

[4]. C.H. Wang, V.K. Dhir, Effect of surface wettability on active nucleation site density durgin pool boiling of water on a vertical surface. J. Heat Trans., 1993b. 115(3):659-669.

[5]. N. Zuber, Hydrodynamic aspects of boiling heat transfer. U.S. AEC Report AECU 4439, June, 1959.

[6]. E. Ruckenstein, Physical model for nucleate boiling heat transfer from a horizontal surface. Bul. Institutului Politech Bucaresti, 1961. 33(3):79-88.

[7]. R. Cole, W. Rohsenow, Correlation of bubble departure diameters for boiling of saturated liquids. Chem. Eng. Prog. Symp. Series, 1968. 65(92):211-213.

[8]. M. Jakob, W. Fritz, Versuche uber den Verdampfungsvorgang. Forsch. Ingenieurwes, 1931. 2:435-447.

[9]. F. Peebles, H. Garber, Studies on motion of gas bubbles in liquids. Chem. Eng. Prog. , 1953. 49:88-97.

[10]. R.F. Gaertner, J.W. Westwater, Population of active sites in nucleation site density in nucleation boiling heat transfer. Chem. Eng. Prof. Symp. Ser., 1960. 56(30):659-669.

[11]. V. Borishanskii, G. Bobrovich, F. Minchenko, Heat transfer from a tube to water and to ethanol in nucleate pool boiling. Symposium of Heat Transfer and Hydraulics in Two-phase Media, Gesenergoizdat, Moscow, 1961.

[12]. T.G. Theofanous, J.P. Tu, A.T. Dinh, T.N. Dinh, The boiling crisis phenomenon Part I: nucleation and nucleate boiling heat transfer. Experimental Thermal and Fluid Science, 2002. 26:755-792.

[13]. T. Raad, J.E. Myers, Nucleation studies in pool boiling on thin plates using liquid crystals. AIChE J., 1971. 17(5):1260-1261.

[14]. D.B.R. Kenning, Wall temperature patterns in nucleate boiling. Int. J. Heat Mass Transfer, 1992. 35(1):73-86.

[15]. C. Gerardi, J. Buongiorno, L.W. Hu, T. McKrell, Infrared thermometry study of nanofluid pool boiling phenomena. Nanoscale Reasearch Letters, 2011. 6:232.

[16]. Y. Iida, K. Kobayasi, Distribution of void fraction above a horizontal heating surface in pool boiling. Bull. JSME, 1969. 12:283-290.

[17]. S.P. Liaw, V.K. Dhir, Void fraction measurements during saturated pool boiling of water on partially wetted vertical surfaces. Trans. ASME, J Heat Transfer, 1989. 111(3):731-738.

[18]. L. Limozin, K.Senqupta, Quantitative Reflection Interference Contrast Microscopy (RICM) in Soft Matter and Cell Adhersion. ChemPhysChem, 2009. 10:2752-2768.

[19]. J. Schilling, K. Senqupta, S. Goennenwein, A. Bausch, E. Sachmann, Absolute interfacial distance measurements by dual-wavelength reflection interference contrast microscopy. Physical Review E, 2004. 69(2):021901.

[20]. P. Robert, K.Senqupta, P. Puech, P. Bongrand, L. Limozin, Tuning the Formation and Rupture of Single Ligand-Receptor Bonds by Hyaluronan-Induced Repulsion. Biophysical Journal, 2008. 95(8):3999-4012.

[21]. C.E. Estrada-Perez, Analysis, comparison and modification of various particle image velocimetry (PIV) algorithms, in Department of Nuclear Engineering. December 2004, Texas A&M University: College Station.

[22]. Y.A. Hassan, T.K.Blanchat, C.H. Seeley Jr, PIV flow visualization using particle tracking techniques. Meas. Sci. Technol., 1992. 3:633-642.

[23]. K. Takehara, T. Etoh, A study on particle identification in PTV particle mask correlation method. Journal of Visualization, 1998. 1(3):313-323.

[24]. C.E. Gharib, M. Gharib, Digital particle image velocimetry. Exp. Fluids, 1991. 10(4):181-193.

[25]. H. Nobach, M. Honkanen, Two-dimensional Gaussian regression for sub-pixel displacement estimation in particle image velocimetry or particle positino estimation in particle tracking velocimetry. Exp. Fluids, 2005. 38(4):511-515.

[26]. J.C. Contreras-Naranjo, J.A. Silas, V.M. Ugaz, Reflection interference contrast microscopy of arbitrary convex surfaces. Applied Optics, 2010. 49(19):3701-3721.

[27]. J. Radler, E. Sackmann, Imaging optical thicknesses and seperation distances of phospholipid vesicles at solid surfaces. J. Phys. II France, 1993. 3:727-748.

[28]. J.S. Ploem, Reflection-contrast microscopy as a tool for investigation of the attachment of living cellls to a glass surface. Mononuclear Phagocytes in Immunity, Infection and Pathology 1975.

[29]. W. R. Barron, Williamson Corporation, Principles of Infrared Thermometry.

[30]. TED PELLA, http://www.tedpella.com/SEMmisc_html/SEMpaint.htm#anchor1335007, 2012.

[31]. 3M. ″Product information, 3M Novec 7000, engineering fluid", website:http://multimedia.3m.com/mws/mediawebserver?mwsId=66666UuZjcFSLXTtlXftMxMVEVuQEcuZgVs6EVs6E666666--. 2009.

[32]. DANTEC Dynamics, http://www.dantecdynamics.com/Default.aspx?ID=731, 2012.

[33]. T. Ferrreita, W. Rasband, Image J User Guide (IJ 1.46r). 9th, September, 2012:1.

[34]. C.D. Gerardi, Investigation of the pool boiling heat transfer enhancement of nano-engineered fluids by means of high-speed infrared thermography. May 2009.

[35]. R. Situ, M. Ishii, T. Hibiki, J.Y. Tu, G.H. Yeoh, M. Mori, Bubble departure frequency in forced convective subcooled boiling flow. International Journal of Heat and Mass Transfer, 2008. 51:6268-6282.

[36]. N. Zuber, Nucleate boiling. The region of osolated bubbles and the similarity with natural convection. Int. J. Heat Mass Transfer, 1963. 6:53-78.

[37]. C. Gerardi, J.Buongiorno, L. Hu, T. McKrell, Study of bubble growth in water pool boiling through synchronized, infrared thermometry and high-speed video. International Journal of Heat and Mass Transfer, 2010. 53:4185-4192.